Mitochondrion 91 (2026) 102174

Contents lists available at ScienceDirect

Mitochondrion

journal homepage: www.elsevier.com/locate/mito

Original Research Article

Mitochondrial dysfunction in muscle cells induced by snoring vibrations

Per Stål [a], Roine El-Habta [a], Yu-Cheng Qian [a], Shaochun Zhu [b], Chloe Williams [a], André Mateus [b,c], Jonathan D. Gilthorpe [a], Farhan Shah [a,*]

[a] Department of Medical and Translational Biology, Johan Bures väg 12, Biologihuset, Umeå universitet, 901 87 Umeå, Sweden
[b] Department of Chemistry, Umeå University, Linnaeus väg 10, Umeå universitet, 901 87 Umeå, Sweden
[c] The Laboratory for Molecular Infection Medicine Sweden (MIMS), Biomedicine Building, Building 6K and 6L University Hospital of Umeå, Umeå universitet, 901 87 Umeå, Sweden

ARTICLE INFO

Keywords:
Muscle cells
Mitochondrial dysfunction
Oxidative phosphorylation
Glycolysis
Vibrations
Snoring
Obstructive sleep apnea

ABSTRACT

Snoring-related vibrations have been proposed as a pathogenic factor contributing to upper airway muscle dysfunction in patients with obstructive sleep apnea (OSA). To investigate whether exposure to snoring vibration is linked to muscle weakness, we used an in vitro vibration model to examine its effects on mitochondrial homeostasis in L6 muscle cells at 8, 12, 24, and 48 h. The findings were then compared with mitochondrial alterations in the upper airway muscles from snorers and patients with OSA. Proteomic analysis of L6 myoblasts revealed extensive remodeling of the mitochondrial proteome at 8 h, affecting pathways involved in oxidative phosphorylation, protein import, ribosome biogenesis, and RNA processing. Respiratory chain remodeling was subunit-specific, with increased abundance of selected components of Complexes I, IV, and V, including NDUFS4, COX5A, and ATP5PD. However, reductions in spliceosome-associated factors, such as SRSF2 and DDX46, along with alterations in mitochondrial ribosomal proteins, indicated impaired RNA processing and protein synthesis. Furthermore, both proteomic and transcriptomic analyses revealed activation of a mechanosensing–mechanotransduction axis, with early upregulation of integrin subunits and mechanosensitive ion channels, followed by transient activation of focal adhesion signaling. Despite transcriptional upregulation of selected Complex IV subunits *Cox5a* and *Cox6a2*, this response was accompanied by accumulation of unspliced pre-mRNA, indicating impaired RNA processing efficiency and a decoupling between transcript and protein levels. Real-time Seahorse assay revealed a collapse of mitochondrial respiration and glycolytic reserve at 8 h. Although mitochondrial oxygen consumption recovered after 48 h, the ability to dynamically upregulate glycolysis remained impaired. In patients, muscle capillarization was impaired, COX activity was reduced, and mitochondrial organization was disrupted. Moreover, transcription of Complex IV subunits *COX5A* and *COX6A2* was, as in vibrated L6 cells, upregulated, suggesting a mismatch between transcript levels and protein expression. We conclude that snoring-induced vibrations are an unrecognized stressor that disrupts mitochondrial homeostasis in muscle by impairing RNA processing, protein synthesis, and mechanotransduction-driven mitochondrial remodeling, leading to transcript–protein uncoupling and likely muscle dysfunction.

1. Introduction

We and others have previously reported neuromuscular changes in the oropharyngeal tissues of long-term snorers, with notable correlations to obstructive sleep apnea (OSA) and swallowing dysfunction (Boyd et al., 2004; Friberg et al., 1998; Jäghagen et al., 2000; Levring Jäghagen et al., 2003; Shah et al., 2018). Interestingly, biopsies from these individuals also revealed muscle fibers with mitochondrial disorganization, reduced oxidative capacity, absence of cytochrome *c* oxidase (COX) activity, abnormalities in a cytoskeletal protein that anchors mitochondria, and reduced capillarization (Shah et al., 2018; Bovenzi, 2005; Murfee et al., 1985; Necking et al., 2004; Waugh et al., 2016; Silver et al., 2018), indicating disturbances in energy metabolism.

Snoring-induced vibrations represent a less-explored but clinically relevant source of repetitive mechanical stress on the upper airway muscles. Long-term occupational exposure to mechanical vibration from

* Corresponding author at: Department of Medical and Translational Biology, Umeå University, SE-901 87 Umeå, Sweden.
E-mail addresses: per.stal@umu.se (P. Stål), roine.el-habta@umu.se (R. El-Habta), yucheng.qian@umu.se (Y.-C. Qian), shaochun.zhu@umu.se (S. Zhu), chloejw96@gmail.com (C. Williams), andre.mateus@umu.se (A. Mateus), jonathan.gilthorpe@umu.se (J.D. Gilthorpe), farhan.shah@umu.se (F. Shah).

https://doi.org/10.1016/j.mito.2026.102174
Received 6 February 2026; Received in revised form 12 May 2026; Accepted 1 June 2026
Available online 2 June 2026
1567-7249/© 2026 The Author(s). Published by Elsevier B.V. This is an open access article under the CC BY license (http://creativecommons.org/licenses/by/4.0/).

hand-held and powered tools is associated with a range of harmful effects on biological tissues, including vascular, neurological, and musculoskeletal disorders (Bovenzi, 2005). Chronic exposure has been linked to muscle fiber atrophy, peripheral neuropathy, impaired blood flow, and muscle weakness (Murfee et al., 1985; Necking et al., 2004). In animal models, vibration exposure is reported to lead to capillary loss, vasospasm, DNA damage, and altered cell signaling, suggesting far-reaching impacts on tissue integrity and cellular function (Waugh et al., 2016). However, the effect of snoring-induced vibrations on energy metabolism in upper airway muscles remains unclear.

Muscle function is energy-dependent and closely linked to mitochondrial health (Silver et al., 2018). Mitochondria generate ATP and maintain oxidative phosphorylation, both of which are critical for proper cellular metabolism. Disruptions to these pathways can compromise muscle contractility and resilience. Changes in the morphology, quantity, and position of mitochondria are a key pathogenic mechanism in a diverse range of diseases and pathologies characterized by dysfunctional mitochondria (Ishihara et al., 2015; Chen et al., 2023; Yapa et al., 2021). Additionally, adequate oxygen delivery is essential for sustaining oxidative metabolism and ATP synthesis (Wheaton and Hypoxia, 2011; Mungai et al., 2011). Thus, vibration-induced disturbances in blood flow may further impair mitochondrial function (Krajnak, 2020; Curry et al., 2002).

The goal of the present study was to use an in vitro model to determine whether snoring-induced vibrations disrupt mitochondrial homeostasis and energy metabolism in muscle cells and to investigate mechanotransduction-related signaling responses. The results were compared with mitochondrial abnormalities in biopsies of upper airway muscles from snoring and OSA patients.

2. Material and methods

2.1. In vitro model

An in vitro experimental model was developed to analyze the effect of snoring vibrations on energy metabolism in cultured muscle cells. The cells were exposed to snoring vibrations for 8, 12, 24, and 48 h to investigate time-dependent alterations at both the gene and protein levels, and for 8 and 48 h to assess mitochondrial respiration and glycolytic flux in real time using the Seahorse assay. Non-vibrated cells maintained under identical conditions served as controls.

2.1.1. Muscle cell culture

The commercial rat muscle cell line L6 (ATCC® CRL-1458™) was used. Myoblasts were cultured in T-175 flasks (Sarstedt, code: 83.3912.002) in Dulbecco's modified Eagle medium (DMEM; Thermo Fisher Scientific, code: 31966021) containing L-alanyl-L-glutamine (GlutaMAX), 10% fetal bovine serum (FBS; Thermo Fisher Scientific, code: 10500064), and 1% penicillin–streptomycin (Thermo Fisher Scientific, code: 15140122). Cultures were maintained at a sub confluent level to maintain the myoblastic component as the cells were passaged.

2.1.2. Coating of cell culture plates

To facilitate cell adhesion, tissue culture plates were treated with poly-D-Lysine (Sigma-Aldrich, code: P6407, 50 μg/ mL) for 1 h followed by rinsing with sterile water. The plates were then coated with rat tail collagen Type I diluted in acetic acid (0.02 N) (Sigma-Aldrich, code: C7661, 50 μg/ cm^2) and left at 4°C overnight. The following day, the collagen solution was aspirated, and culture plates were rinsed with sterile water. L6 cells were seeded at a density of 300,000 cells per well in a 6-well plate (Corning, code: 353504).

2.1.3. Experimental setup

The culture plates were firmly attached to a metallic frame placed above a 12-inch subwoofer loudspeaker (MDS, Stockholm). The loudspeaker, rated at 1000 W, was driven by a low-frequency (LF) amplifier connected to a laptop (Dell Technologies, USA) and operated using a 30-second looping snoring sound file (.wav) recorded from one of the patients included in the study. This setup was used to subject the cultured cells to vibrations. To measure the acceleration generated by the snoring vibrations on the cell culture plate, an ADXL 345 accelerometer (Analog Devices, Inc., Wilmington, MA) was attached to the vibrating platform. Additionally, the vibrations reaching the base of the cell culture wells were confirmed using a Digiducer 333D01 (SN81419) accelerometer (Modal Shop, Inc., USA).

2.1.4. Recording, analysis, and experimental application of snoring sound

Snoring sound was recorded by the built-in microphone on Nox T3 (Nox-T3, Nox Medical Inc) strapped to the chest of the patient used. Built-in microphones for Nox T3 were checked against a calibrated industrial sound level meter (REED EC-05 Sound level calibrator) using a frequency sweep from 50-4000 Hz. The saturation for audio signal on T3 device was set at 106.4 dB, since it is highly unlikely that snoring sounds are produced above 105 dB. For the expected bands of major interest to audio power of snoring maximum deviation was −3 dB.

The snoring sound recording was clipped to a loop for 30 s. For analysis of energy spectrum in the recorded snoring sound loop of 30 s, sound file.wav was exported to MATLAB (the MathWorks, Inc. R2021a) for the FFT (fast Fourier transform) transformation. Fig. 1 A shows the 30 s acoustic signal of snoring sound where time and amplitude are plotted. These snoring sounds show large amplitude variations at time intervals of 5, 10, 15, 23 and 26 s. The power spectrum (%) of the 30-second sound file was acquired using FFT (0–2000 Hz); the energy peaks were observed between 50–400 HZ and 1000–1400 Hz with a maximum energy peak around 100 Hz (Fig. 1 B). The maximum acceleration achieved on the surface of the culture plate was 3.2 g. The snoring vibration model system was placed inside a conventional culture/incubator chamber at 37°C and 5% CO2. L6 cells were subjected to a snoring vibration loop for 8, 12, 24, or 48 h. Corresponding non-vibrated control cells were maintained under identical conditions for the same time points before analysis.

2.1.5. Proteomics

To analyze changes in protein synthesis in muscle cells, cellular proteins were digested into peptides using a modified SP3 protocol (Hughes et al., 2014; Hughes et al., 2019). Briefly, L6 muscle cell pellets were resuspended in lysis buffer (2% SDS, 20 mM Tris(2–carboxyethyl) phosphine hydrochloride) and boiled at 95°C for 10 min. SpeedBeads magnetic carboxylate modified particles (Sigma Aldrich, beads A hydrophylic, cat.no GE45152105050250; beads B hydrophobic, cat.no GE65152105050250,) were combined with ratio 1:1 v/v and washed using liquid chromatography mass spectrometry grade (LC-MS water, four times. Then the beads were mixed with each sample in binding buffer (50% ethanol and 2.5% formic acid) and incubated with shaking at 500 rpm for 15 min at room temperature. Then they were transferred into one filter plate (0.22 μm, Sigma Aldrich, part.no: MSGVN2210). Unbound fraction was removed by centrifugation at 1000 xg. Beads were retained on the filter and washed with 70% ethanol four times. Trypsin was mixed with digestion solution (100 mM HEPES pH7.5, 5 mM chloroacetamide, 1.2 mM TCEP) and added to each sample (1 μg trypsin was used for 25 μg protein) on the plate. Samples were digested overnight at room temperature with shaking at 500 rpm. Flow-through containing the peptides was collected with centrifugation at 1000 xg. Dimethyl sulfoxide (DMSO; 10 μl of 2% solution) was added to beads for eluting bound peptides and pooled with the previous flowthrough. Peptides were desalted by the Oasis HLB plate (Waters, code: 186001828BA) using the manufacturers' protocol and then dried by SpeedVac.

Liquid chromatography tandem mass spectrometry (LC-MS/MS) was used for analysis. Dried peptides were dissolved with 0.1% formic acid in water. Peptides from each sample (1 μg) were introduced to using the Vanquish Neo (Thermo Fisher Scientific). The trapping column used was

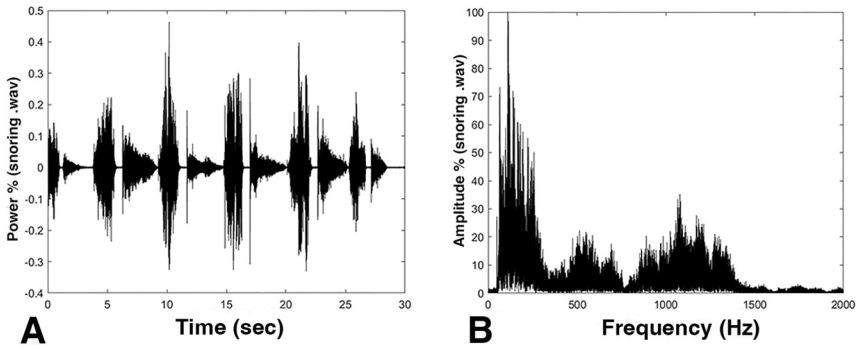


Fig. 1. Characterization of snoring sound vibrations used in the in-vitro vibration model. (A) A 30-second segment of the acoustic snoring signal recorded from a patient during sleep. The amplitude-time waveform displays substantial variation, with particularly prominent high-amplitude oscillations occurring at approximately 5, 10, 15, 23, and 26 seconds, indicating irregular vibration bursts. These fluctuations reflect non-harmonic, transient airflow disruptions in the upper airway, likely caused by the airway walls collapsing during inspiration. (B) Power spectral density (PSD) of the 30-second snoring signal was computed using Fast Fourier Transform (FFT). The spectrum reveals two dominant energy bands: a low-frequency range (50–400 Hz) with a peak near 100 Hz, and a higher-frequency range between 1000–1400 Hz. These frequency components correspond to tissue vibration and possibly fluttering phenomena of pharyngeal structures. The observed spectral pattern suggests that different parts of the airway are vibrating in varied ways during snoring.

a PEPMAP NEO C18 (5 μm particle size, 300 μmx5mm, Thermo Scientific). The analytical column used was a nano Ease^{TM} M/Z HSS C18 T3 (100Å, 1.8 μm particle size, 75 μm x 250 mm, Waters). A total time of 120 min was used for separation and elution was performed with a gradient of mobile phase A (water and 0.1% formic acid) to 8% B (80% acetonitrile and 0.1% formic acid) over 4 min and to 27% B over 87 min, then to 80% B for 0.1 min and hold for 4 min, finally to 2% B for 0.5 min and finally, column equilibration was performed.

Data acquisition was carried on an Exploris 480 (Thermo Scientific) using a data-dependent method. Survey scans covering the mass range of 375 – 1500 were acquired at a resolution of 120,000, RF lens of 40%, and normalized automatic gain control (AGC) of 300%. A maximum cycling time of 2 s was used to control the number of precursors for tandem mass spectrometry (MS^2) analysis. Charge states include 2–6 charges. Dynamic exclusion was set to exclude the previously selected precursors for 35 s. mass spectrometry (MS) scans were acquired at a resolution of 15,000 (at *m/z* 200), with Automatic Gain Control (AGC) target value of auto. The isolation window was 1.4 *m/z*. Higher Energy Collisional Dissociation (HCD) fragmentation was induced with a normalized collision energy (NCE) of 30. Isotopes were excluded for MS^2 analysis.

2.1.6. Proteomics data analysis

Raw data was searched against the *Rattus norvegicus* UniProt FASTA (proteome identifier [ID] UP000002494) using FragPipe (version 18), label free quantification was achieved using LFQ-MBR workflow. FragPipe-Analyst was used for statistics analysis (https://fragpipe-analyst.nesvilab.org/). To reduce technical variation, data was normalized by variance stabilizing normalization method using vsn package (Huber et al., 2002). Missing values were replaced with the minimum value in each sample and FDR correction was performed using Benjamini Hochberg method.

2.1.7. Enrichment analysis

Proteomics data were subjected to functional annotation and pathway enrichment analysis using the g:Profiler toolset (Raudvere et al., 2019). Lists of significantly dysregulated proteins (adjusted p-value < 0.05) were generated separately for each timepoint (8 h, 12 h, 24 h, and 48 h vibration vs control comparisons) and used as input for the g:GOSt functional profiling module. The analysis included multiple annotation sources, Gene Ontology (GO), Biological Process (BP), Cellular Component (CC), Molecular Function (MF), Kyoto Encyclopedia of Genes and Genomes (KEGG), Reactome, WikiPathways, and the Human Phenotype Ontology (HPO), with the organism set to *Rattus norvegicus*. Enrichment results were calculated using g:Profiler's hypergeometric test with Benjamini–Hochberg FDR (false discovery rate) correction for multiple comparisons. For each time point, significantly enriched terms (adjusted p-value < 0.05) were retained for downstream interpretation and comparison across the temporal profile.

2.1.8. Gene expression analysis using real-time quantitative PCR

To analyze changes in the genes of Complex I and Complex IV in the mitochondrial respiratory chain, total RNA was extracted from cells cultured in 6-well plates using the RNeasy Mini Kit (Qiagen, code: 74106) according to the manufacturer's instructions. cDNA was synthesized from 1 μg RNA using the High-Capacity cDNA Reverse Transcription Kit (Applied Biosystems; code: 4368813). RT-qPCR was performed using TaqMan Gene Expression Assays (Applied Biosystems) and ViiA 7 Real-Time PCR System (Applied Biosystems). Probes included cytochrome *c* oxidase subunit 5A (*Cox5a*; Applied Biosystems; code: Rn00821806), cytochrome *c* oxidase subunit 6A2 (*Cox6a2*; Applied Biosystems; code: Rn00689038), *Cox6c* (Applied Biosystems; code: Rn00820983), and NADH dehydrogenase [ubiquinone] iron-sulfur protein 4 (*Ndufs4*; Applied Biosystems; code: Rn01489307). Thermal cycling conditions were 50°C for 2 min, 95°C for 20 s followed by 40 cycles of 95°C for 1 s, and 60°C for 20 s. Data were analyzed with ViiA 7 software (Applied Biosystems). Ribosomal protein L13a (*Rpl13a*; Applied Biosystems; code: Rn00821946) was used as an internal control.

Transcriptional responses related to mechanotransduction, mitochondrial dynamics, RNA processing, and apoptosis were assessed by RT-qPCR. RNA extraction and cDNA synthesis were performed as described previously. Reactions were run using FastStart Universal SYBR Green Master (ROX; Roche, 90376800) under standard cycling conditions (95°C for 10 min; 40 cycles of 95°C for 10 s and 60°C for 30 s). Primers (Table 3) were validated for efficiency and specificity. Gene expression was normalized to *Rpl13a* and β-actin and calculated using the $2^{-}\Delta\Delta Ct$ method. To evaluate RNA processing efficiency, unspliced pre-mRNA of *Cox5a* and *Cox6a2* (mitochondrial Complex IV subunits) was quantified using primer pairs designed to amplify intron-containing regions, enabling specific detection of pre-mRNA transcripts. Upstream mechanosensory components were assessed using integrin subunit beta 1 (*Itgb1*), integrin subunit alpha 7 (*Itga7*), and piezo-type mechanosensitive ion channel component 1 (*Piezo1*), while downstream mechanotransduction signaling was evaluated using protein tyrosine kinase 2 (*Ptk2*) and the cytoskeletal regulator actinin alpha 4 (*Actn4*). Mitochondrial dynamics were analyzed using dynamin 1-like protein

(*Dnm1l*), mitofusin 1 (*Mfn1*), mitofusin 2 (*Mfn2*), and optic atrophy 1 (*Opa1*). Cellular stress and apoptotic signaling were assessed using BCL-2 associated X protein (*Bax*), BCL2 binding component 3 (*Bbc3*), B-cell lymphoma 2 (*Bcl2*), caspase 9 (*Casp9*) and caspase 3 (*Casp3*).

2.1.9. Cellular senescence β-galactosidase staining

Cellular senescence was assessed using a β-galactosidase staining kit (Abcam, ab65351) according to the manufacturer's instructions. Briefly, cells were fixed and incubated with β-galactosidase staining solution. After staining, cells were mounted using an antifade mounting medium containing DAPI (Vector Laboratories, H-1200) to visualize cell nuclei.

Stained cells were imaged at 20x magnification using brightfield and fluorescence microscopy. Senescent cells were identified by the presence of blue β-galactosidase staining under brightfield microscopy, while total cell number was determined by DAPI nuclear staining.

Quantification was performed using Image J software (National Institutes of Health, Bethesda, MD, USA) The percentage of senescent cells was calculated as the number of β-galactosidase–positive cells relative to the total number of cells in randomly selected fields (three fields per well, four wells per condition; n = 4).

2.1.10. Seahorse assays

Based on proteomic and transcriptomic profiling, which identified 8 h of vibrations as the peak of molecular disruption and 48 h as the point of maximal adaptive remodeling, these time points were selected for functional analysis. Following exposure to snoring vibrations, the Seahorse mitochondrial stress (Mito Stress) assays were performed using a Seahorse XFp Bioanalyser to assess both oxidative and glycolytic activity in L6 cells at 8 and 48 h, using real-time measurements of oxygen consumption rate (OCR) and extracellular acidification rate (ECAR), respectively. Twenty-four hours prior to cell seeding, 8-well Seahorse XFp Cell Culture Miniplates (Agilent Technologies, code: 103025–100) were coated with poly-D-lysine and collagen (as above). L6 cells were seeded at 40,000 cells/well and incubated at 37°C in a 5% CO2 incubator for 24 h. The cells were then subjected to control conditions or snoring vibrations for 8 h and 48 h. Seahorse sensor cartridges (Seahorse XFp FluxPak, Agilent Technologies, code: 103022100) were hydrated with 200 μl of deionized water per well and incubated overnight a 37°C in a non-CO2 incubator. On the morning of the assay, the deionised water was replaced with 200 μl of Seahorse XF Calibrant Solution (Agilent Technologies, code: 103059–000) Mito Stress assay media consisted of low-buffered Dulbecco's Modified Eagle's Medium (DMEM; Sigma-Aldrich, code: D5030) was supplemented with glutamine (Thermo Scientific, code: 25030123, 2 mM), glucose (Sigma-Aldrich, code: G7021, 10 mM) and pyruvate (Sigma-Aldrich, code: P5280, 1 mM; freshly prepared from sodium pyruvate powder). The media was equilibrated to 37°C in a non-CO2 incubator and the pH was adjusted to pH 7.4 using 1 M NaOH. The cells were washed (twice with 200 μL/well) and incubated in 180 μL per well of assay media for 1 h at 37°C in a non-CO2 incubator prior to the assay. For Mitostress assays, oligomycin (Sigma-Aldrich, code: 495455), carbonyl cyanide 4-(trifluoromethoxy) phenylhydrazone (FCCP, Sigma-Aldrich, code: C2920) and rotenone/antimycin A (Sigma-Aldrich, code: R8875/A8674) were made at 10X concentration (10 μM, 20 μM and 5 μM, respectively).

Each measurement cycle lasted 3 min. Three baseline measurements were taken prior to the addition of each compound, and subsequently, three measurements were taken afterward. OCR and ECAR were reported as absolute rates (pmol/min for OCR and mpH/min for ECAR). Data was exported from the Seahorse XFp Extracellular Flux Analyser into Seahorse XF Report Generator software for analysis.

2.2. Analyzes of samples from snoring and OSA patients

To determine whether the alterations observed in the in vitro vibration model were also present in the upper airway muscles of snoring and OSA patients, muscle biopsies were analyzed for expression of proteins and genes associated with mitochondrial complex IV and for parameters reflecting the capillary perfusion capacity of muscle fibers.

2.2.1. Patients and healthy subjects

The study included 19 patients (1 female, 18 males), mean age 47 years (range 21–77 years), and mean BMI 28 kg/m^2 (range 21–33), who were referred for soft palate surgery following a clinical examination confirming snoring with or without OSA. The exclusion criteria were smoking, previous palatal surgery, systemic disease, medications, and drug abuse. Five healthy male controls, mean age 55 years (range 47–77), and a mean BMI of 30 kg/m^2 (range 27–32 kg/m^2), were included in the study. Exclusion criteria were the same as in patients but also included habitual snoring and OSA.

2.2.2. Clinical investigation and sleep apnea recordings

All patients and controls underwent a type 3 study. The portable ambulatory overnight sleep apnea device (Embletta, Embla Systems, Kanata, Canada) recorded continuous signals for airflow via nasal cannula pressure, thoracic and abdominal respiratory movements, snoring sounds, finger pulse oximetry (Nonin Oximeter Xpod, Nonin Medical Inc. Plymouth), and body position. Recordings were performed for a minimum of 4 h during sleep (average sleep time was 6.3 h for patients and 6.6 h for healthy subjects) and were manually scored according to the American Academy of Sleep Medicine (AASM) guidelines. An apnea was defined as a ≥90% cessation of airflow lasting at least 10 s, while a hypopnea was defined as a 50% reduction in airflow from baseline, combined with an oxygen desaturation of ≥3% (Coste et al., 2010).

According to overnight sleep registration, all 19 patients had a history of snoring (mean duration 20 years; range 6–40 years), and 15 had OSA. The mean apnea–hypopnea index (AHI) was 17.8 (range: 1.5–84).

2.2.3. Muscle samples

Muscle samples from the base of the uvula were obtained in patients undergoing soft palate surgery. In the voluntary control subjects, samples were taken from the corresponding area using the punch biopsy technique.

2.2.4. Immunohistochemistry

The muscle samples were oriented and mounted for cross-sectioning in OCT compound (Tissue Tek, Miles, Elkhart, IN, USA) and frozen in liquid propane chilled with liquid nitrogen. Serial muscle sections, 5 μm thick, were cut at −20° in a cryostat and mounted on glass slides. The sections were immunostained with previously characterized monoclonal (mAb) and polyclonal antibodies directed against cytoskeletal, basement membrane, and three mitochondrial proteins (Table 1). The antibody TOMM20, which recognizes a transit peptide receptor on the mitochondrial outer membrane, was used to assess mitochondrial content and localization in muscle fibers. Abnormalities in mitochondrial activity within muscle fibers were assessed using mAb anti-MTCO2, which targets COX subunit 2, a component of Complex IV in the mitochondrial respiratory chain, and mAb anti-COX IV, which targets a COX subunit in Complex IV. To visualize the basement membranes of both muscle fibers and capillaries, sections were stained with a polyclonal antibody against laminin, a major component of the basal lamina.

Bound primary Abs were visualized by indirect immunofluorescence using affinity-purified secondary Abs prepared for multiple labeling and conjugated with fluorochromes with different emission spectra; fluorescein isothiocyanate (FITC), Rhodamine Red-X (RRX; Jackson ImmunoResearch Laboratories, West Grove, PA, USA), Alexa Fluor 488, and Alexa Fluor 647 (Invitrogen, CA, USA). The sections were then washed in PBS for 3 x 5 min and mounted in Vectashield Mounting Medium (H-1000) (Vector Laboratories, Burlingame, CA, USA). Negative control sections were treated as above, except that the primary Abs were replaced with non-immune serum. For details of the multi-staining technique, see (Shah et al., 2016).

Table 1
Antibodies used for immunohistochemistry.

Antibody	Product Code	Specificity	Gene*	Host/Clone	Dilution	Source
Anti-TOMM20 Mitochondrial Marker	ab186735	Human and animal mitochondria	TOMM20	pAb (rabbit)	1:1000	1
Anti-COX IV Mitochondrial Marker	Ab33985	Human and animal mitochondria	COX4I1	mAb (mouse)	1:5000	1
Anti-MTCO2 Mitochondrial Marker	Ab3298	Human and animal mitochondria	MTCO2	mAb (mouse)	1:250	1
Laminin	PC 128	Human laminin	LAMININ	pAb (sheep)	1:15000	2

*Official gene nomenclature according to OMIM. (http://www.ncbi.nlm.nih.gov/omim/); 1. Abcam, UK,; 2. Binding site Inc, USA; 8. Santa Cruz Biotechnology Inc. UK,

2.2.5. Enzyme-histochemistry

Using double histochemical staining for COX and succinate dehydrogenase (SDH) (EC 1.3.99.1), an enzyme complex involved in the oxidative phosphorylation chain and the tricarboxylic acid cycle (TCA) cycle, deficits in the mitochondrial respiratory chain were assessed. COX-positive fibers stained brown, and fibers lacking COX activity stained blue.

2.2.6. Analysis of mitochondria distribution and capillarization of muscle fibers

Four to five random areas from each muscle cross-section were scanned at 20x magnification with a fluorescence microscope (Leica DM6000B, Leica Microsystems CMS GmbH, Wetzlar, Germany) equipped with a digital high-speed fluorescence charge-coupled device (CCD) camera (Leica DFC360 FX). In cross-sections stained for the mitochondrial COX2 subunit (mAb MTCO2), muscle fibers were subdivided based on staining intensity (unstained, weakly, moderately, or strongly stained) and on the normal or abnormal mitochondrial distribution pattern. The cross-sectional area of each muscle fiber (fCSA) and capillaries was measured by tracing the circumference of the muscle and capillary membranes stained for pAb Z0097 against laminin using morphometric software Leica QWin (Standard version 3.5.1 software; Leica Microsystems Ltd). The measurements included capillary density (cap/mm^2), the number of capillaries around each fiber (CAF), and CAF related to fiber cross-sectional area (CAFA), calculated as CAF/fCSA x 10^3. All capillaries within 5 μm of each individual muscle fiber were included in the calculations. The investigators were blinded to the identity of the samples.

2.2.7. Gene expression analysis using real-time quantitative PCR

For RT-qPCR, samples from 5 patients showing typical morphological muscle alterations were used (mean age 55 years, range 47–77, mean BMI 30.6 kg/m^2 range 28–32 kg/m^2, mean AHI 20, range 10–26). Unfixed muscle biopsies were homogenized in QIAzol (Qiagen; code: 79306) using a handheld tissue disruptor. The homogenate was placed on the benchtop for 5 min to promote the dissociation of nucleoprotein complexes. Chloroform was then added to the tube (at a ratio of 1:5) and shaken vigorously for approximately 15 s. The homogenate was centrifuged at 18 600xg at 4°C for 15 min, after which the upper aqueous phase was transferred to a new tube and mixed with 1.5 vol of 100% ethanol. Total RNA was purified using the RNeasy Mini Kit (Qiagen; code: 74106) according to manufacturer's instructions; cDNA was synthesized using the High-Capacity cDNA Reverse Transcription Kit (Applied Biosystems; code: 4268813); and RT-qPCR was performed with TaqMan Gene Expression Assay (Applied Biosystems). The amplification was performed on a ViiA 7 Real-time PCR system (Applied Biosystems). Thermal cycling conditions were 50°C for 2 min, 95°C for 20 s, and 40 cycles of 95°C for 1 s, and 60°C for 20 s.

Based on findings from the in vitro vibration model, the expression of specific genes within mitochondrial complex IV was examined in human muscle samples using probes targeting COX subunits: *COX5A* (Applied Biosystems; code: Hs00362067) and *COX6A2* (Applied Biosystems; code: Hs00193226). Data were analyzed with ViiA 7 software (Applied Biosystems) and PCR Array Analysis Web Portal (Qiagen). The expression levels were normalized to β-actin (Applied Biosystems; code: Hs01060665).

2.2.8. Statistical analysis

Statistical tests for human samples and qPCR were performed using SPSS version 26 (IBM SPSS Statistics, IBM Corporation). Normality in the distribution of data was tested by using the Shapiro-Wilk test. Comparisons between the groups were made using the independent sample *t*-test for variables with normal distribution; the Mann-Whitney *U* test was performed for variables with non-normal distribution. Values are presented as mean ± SD. The results were considered significant at P values ≤ 0.05. Seahorse XF data were analyzed in GraphPad Prism. OCR and ECAR time-course curves were compared using two-way repeated measures ANOVA (or a mixed-effects model if missing values occurred). Derived parameters, non-mitochondrial oxygen consumption, basal respiration, ATP production, maximal respiration, spare respiratory capacity, coupling efficiency, and proton leak, were analyzed by one-way ANOVA with appropriate post hoc tests, or by Kruskal–Wallis with Dunn's test when assumptions of normality were not met. A p value ≤ 0.05 was considered statistically significant.

3. Results

3.1. In vitro model

3.1.1. Proteomic dysregulation and pathway analysis

Proteomic analysis was conducted to compare changes in protein expression across 8, 12, 24, and 48 h of vibration exposure. Out of the 3,391 proteins quantified, a substantial fraction of the quantified proteome showed significant changes (adjusted $p < 0.05$), including many proteins with $|\log_2 FC| > 1$. Of these, 615 mapped to functional categories in g:Profiler and were used for downstream pathway enrichment analysis (Fig. 2 volcano plots). The most significantly enriched pathways included oxidative phosphorylation, carboxylic and amino acid metabolism, mitochondrial protein import, ribosome/translation, spliceosome, and regulation of apoptosis, highlighting coordinated disruption of energy metabolism, RNA processing, and proteostasis (see Table 2 for fold changes and adjusted p values).

3.1.2. Oxidative phosphorylation (OXPHOS)

Analysis of respiratory chain proteins revealed subunit-specific remodeling across complexes. Within Complex IV, the COX subunit 5A showed a consistent and significant increase across all time points, while COX6C2 exhibited a delayed increase at 48 h. COX7A2 displayed a biphasic pattern, with increased abundance at 8 h, transient normalization at 12 h, and renewed upregulation at 24 and 48 h. COX6A2 was

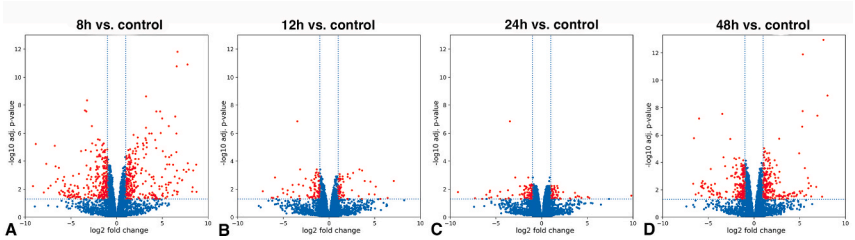


Fig. 2. Volcano plots showing proteomic changes after 8–48 h of snoring-induced vibrations in L6 muscle cells. Volcano plots showing differential protein abundance after 8, 12, 24, and 48 h of snoring-induced vibration exposure in L6 muscle cells relative to controls. Blue dots denote significantly regulated proteins (adjusted $p < 0.05$, $|\log_2 \text{fold change}| \geq 1$), and red dots indicate non-significant proteins. Vertical dotted lines indicate the $\log_2$ fold-change thresholds (± 1), while the horizontal dotted line represents the statistical significance cutoff (adjusted $p = 0.05$).

not detected in the proteomics dataset, likely due to low abundance. Within Complex I, several subunits showed increased abundance at later time points. NADH–ubiquinone oxidoreductase (Complex I) subunits NDUFS4 and NDUFS6 were significantly elevated at 24 and 48 h, whereas NDUFS1 showed a significant increase only at 48 h. These findings indicate preferential accumulation of multiple Complex I core subunits during prolonged vibration exposure.

Several ATP synthase subunits in Complex V, which together catalyze mitochondrial ATP production, showed significant increases in abundance, predominantly at later time points. ATP5PD, an F_0-associated peripheral stalk subunit, and ATP5PO, an F_1-associated subunit, were significantly increased at all time points. In addition, several core F_0 and F_1 catalytic subunits showed significant increases at 24 and 48 h (see Table 2).

3.1.3. Glycolysis and metabolic coupling

Proteomic analysis revealed significant alterations in glycolytic enzymes. Among phosphofructokinase (PFK) isoforms, which catalyze the principal rate-limiting step of glycolysis, PFKL (liver-type phosphofructokinase) was significantly reduced across all time points, indicating impaired control of glycolytic flux.

Several downstream glycolytic enzymes were also significantly reduced. Glyceraldehyde-3-phosphate dehydrogenase (GAPDH), aldolase A (ALDOA), phosphoglycerate kinase 1 (PGK1), and pyruvate kinase M (PKM) exhibited significant downregulation across all time points, with sustained downregulation at 48 h.

Enzymes involved in lactate metabolism were likewise affected. Lactate dehydrogenase A (LDHA) was significantly downregulated across all time points, suggesting impaired NAD^+ regeneration and redox-balancing capacity.

3.1.4. Mitochondrial transporters

Transport proteins showed diverse patterns of regulation. The mitochondrial glutamate carrier SLC25A22 was significantly suppressed at 8 and 12 h, indicating an early reduction in amino acid transport capacity that was not sustained at later time points. In contrast, the adenine nucleotide translocator 1 (SLC25A4/ANT1) increased significantly at 12 h, suggesting a transient enhancement of ADP/ATP exchange during early adaptation. These opposing responses point to selective remodeling of mitochondrial transport functions.

3.1.5. Chaperone and proteostasis pathways

Stress-responsive chaperones displayed compartment-specific regulation. Cytosolic heat shock protein 90 isoforms HSP90AA1 and HSP90AB1 were consistently downregulated across all time points. By contrast, mitochondrial chaperone HSPE1 was significantly upregulated at all time points, and HSPA9 was upregulated at 8, 12, and 24 h.

3.1.6. RNA processing and splicing

Key regulators of RNA metabolism were dysregulated following vibration exposure. Several spliceosome-associated factors, including serine/arginine-rich splicing factor 2 (SRSF2) and DEAD-box helicase 46 (DDX46) was significantly downregulated across all time points. In addition, SUB1, which links transcription to RNA processing, was significantly downregulated at 8, 12, and 24 h.

The core spliceosomal component small nuclear ribonucleoprotein polypeptide C (SNRPC) showed modest upregulation across multiple time points, highlighting heterogeneous regulation of RNA-processing machinery rather than uniform suppression.

3.1.7. Mitochondrial ribosomal proteins

Proteomic analysis showed a significant increase in mitochondrial ribosomal large-subunit proteins MRPL37 (8–24 h) and MRPL22 (12–24 h).

3.1.8. Cell membrane–associated mechanosensing

Upstream membrane-associated mechanosensors, including the integrin subunits ITGB1 and ITGA7, were consistently upregulated across time points. ITGB1 was significantly increased ($p < 0.05$) at 8, 12, and 24 h with a sustained upward trend at 48 h. Similarly, ITGA7 was significantly upregulated at 8 and 48 h ($p < 0.05$) with a non-significant but consistent increase at 12 and 24 h time points. The mechanosensitive ion channel PIEZO1 exhibited a consistent upward trend across all time points, although not significant.

3.1.9. Intracellular mechanotransduction signaling

The focal adhesion kinase PTK2 showed a significant ($p < 0.001$) increase at 8 h, followed by a significant reduction at 24 and 48 h ($p < 0.01$), indicating a transient early activation of mechanotransduction signaling. The cytoskeletal regulator ACTN4 showed a modest decrease across time points, reaching statistical significance only at 48 h ($p = 0.014$).

3.1.10. Mitochondrial dynamics (fission/fusion)

The mitochondrial fission protein DNM1L showed a progressive decrease, reaching statistical significance ($p = 0.046$) at 24 h. In contrast, the mitochondrial fusion protein MFN1 was consistently and significantly upregulated across all time points ($p < 0.05$), indicating enhanced fusion-related activity. MFN2 did not show significant changes at any time point. The inner mitochondrial membrane regulator OPA1 displayed a gradual increase, although this did not reach statistical significance (see Table 2).

3.1.11. Apoptotic signaling (mitochondrial pathway)

The pro-apoptotic proteins BBC3 and BAX showed no detectable change at the protein level across all time points. The executioner caspase CASP3 and anti-apoptotic protein BCL2 displayed a significant decrease at 8 h. BCL2 showed a tendency to upregulation at 12, 24, and 48 h (see Table 2 for fold changes and adjusted p values).

3.1.12. Mitochondrial gene expression in L6 muscle cells

To complement the proteomic findings, we examined transcript levels of key mitochondrial subunits from Complex I and Complex IV in L6 muscle cells following vibration exposure.

Table 2
Proteomic remodeling of mitochondrial pathways following snoring-induced vibration.

Pathway	Protein	8 h (log_2FC, adj. p)	12 h (log_2FC, adj. p)	24 h (log_2FC, adj. p)	48 h (log_2FC, adj. p)	Functional implication
Oxidative phosphorylation – Complex IV	COX5A	+0.756, p = 0.006	+0.797, p = 0.012	+0.819, p = 0.012	+0.549, p = 0.03	Sustained upregulation of a Complex IV subunit, consistent with subunit-level remodeling
	COX7A2	+0.855, p = 0.03	+0.534, p = 0.204	+0.737, p = 0.073	+1.61, p = 0.0013	
	COX6C2	+0.484, p = 0.058	+0.286, p = 0.301	+0.435, p = 0.103	+0.52, p = 0.044	
Oxidative phosphorylation – Complex I	NDUFS1	+0.0816, p = 0.63	+0.245, p = 0.16	+0.321, p = 0.062	+0.646, p = 0.0015	Accumulation of a Complex I core subunit involved in electron transfer
	NDUFS4	+0.0797, p = 0.71	+0.283, p = 0.185	+0.558, p = 0.021	+0.551, p = 0.01	Accumulation of an assembly-associated Complex I subunit linked to complex stability
	NDUFS6	+0.292, p = 0.44	+0.676, p = 0.113	+0.839, p = 0.048	+1.03, p = 0.013	Accumulation of a Complex I N-module subunit during complex remodeling
ATP synthase (Complex V)	ATP5PD	+0.475, p = 0.003	+0.495, p = 0.0076	+0.629, p = 0.0059	+0.454, p = 0.0046	Structural stabilization of ATP synthase (peripheral stalk)
	MT-ATP8	+0.426, p = 0.127	+0.144, p = 0.659	+0.749, p = 0.026	+0.384, p = 0.172	Structural support of the membrane-embedded ATP synthase complex
	ATP5PO	+0.326, p = 0.051	+0.438, p = 0.031	+0.537, p = 0.013	+0.454, p = 0.012	Accessory regulation of ATP synthase assembly and stability
	ATP5ME	+0.468, p = 0.077	+0.337, p = 0.249	+0.59, p = 0.048	+0.556, p = 0.041	Modulation of ATP synthase oligomerization and cristae architecture
	ATP5F1A	+0.194, p = 0.252	+0.252, p = 0.176	+0.394, p = 0.044	+0.447, p = 0.016	Increased abundance of catalytic F_1 subunits of ATP synthase
	ATP5F1B	+0.114, p = 0.451	+0.186, p = 0.257	+0.368, p = 0.034	+0.114, p = 0.012	Catalytic ATP synthesis capacity (F_1 sector)
	ATP5F1C	+0.282, p = 0.131	+0.377, p = 0.081	+0.451, p = 0.039	+0.611, p = 0.0056	Subunit involved in coupling proton translocation to ATP synthesis
	ATP5IF1	−0.0526, p = 0.864	+0.254, p = 0.318	+0.594, p = 0.030	+0.669, p = 0.010	Increased abundance of ATP synthase inhibitory factor
Glycolysis	PFKL	−0.966, 0.0195	−1.05, 0.029	−0.855, 0.0495	−0.185, 0.0412	Reduced glycolytic flux control
	GAPDH	−1.23, p < 0.001	−0.796, p < 0.01	−0.666, p < 0.01	−0.796, p < 0.001	Reduced central glycolysis
	ALDOA	−0.64, p < 0.01	−0.476, p = 0.017	−0.568, p < 0.01	−0.783, p < 0.001	Limits downstream glycolytic flux
	PGK1	−0.58, p = 0.001	−0.324, p = 0.049	−0.425, p = 0.016	−0.675, p < 0.001	Reduced substrate-level ATP generation
	PKM	−1.02, p < 0.001	−0.507, p < 0.01	−0.588, p < 0.01	−0.9, p < 0.001	Reduced terminal ATP production in glycolysis
	LDHA	−1.03, p < 0.001	−0.623, p = 0.013	−0.704, p < 0.01	−0.796, p < 0.001	Impaired NAD^+ regeneration for glycolysis
Mitochondrial transport	SLC25A22	–1.91, p = 0.0056	–1.58, p = 0.032	–0.512, p = 0.42	–0.179, p = 0.804	Reduced amino acid import
	SLC25A4 (ANT1)	+0.367, p = 0.216	+1.13, p = 0.0066	+0.447, p = 0.152	+0.564, p = 0.062	Increased abundance of the ADP/ATP exchanger ANT1
Proteostasis / chaperones	HSP90AA1	−0.869, p = 0.000358	−0.521, p = 0.019	−0.719, p = 0.00643	−1.01, p = 0.000358	Reduced cytosolic protein-folding capacity
	HSP90AB1	−0.846, p = 0.000236	−0.615, p = 0.0060	−0.736, p = 0.00593	−0.914, p = 0.000251	
	HSPE1	+0.557, p = 0.0021	+0.654, p = 0.0029	+0.641, p = 0.005	+0.453, p = 0.007	Upregulation of mitochondrial protein-folding machinery
	HSPA9	+0.369, p = 0.016	+0.479, p = 0.011	+0.423, p = 0.019	+0.161, p = 0.259	Transient enhancement of mitochondrial protein import and folding
RNA processing / splicing	SRSF2	–0.821, p = 0.006	–0.702, p = 0.032	–0.629, p = 0.039	–0.574, p = 0.0361	Impaired spliceosome function
	DDX46	–0.856, p = 0.025	–0.883, p = 0.006	–0.918, p = 0.007	–0.694, p = 0.008	Reduced splicing efficiency
	SUB1	–1.89, p = 0.00125	–1.58, p = 0.01	–1.08, p = 0.041	–0.349, p = 0.463	Disruption of transcription–RNA processing coupling
	SNRPC	+0.409, p = 0.036	+0.313, p = 0.137	+0.539, p = 0.0217	+0.424, p = 0.0308	Altered core spliceosome composition
Mitochondrial ribosome	MRPL22	+0.411, p = 0.058	+0.642, p = 0.0187	+0.538, p = 0.032	+0.344, p = 0.109	Altered mitochondrial ribosomal composition
	MRPL37	+0.504, p = 0.029	+0.599, p = 0.03	+0.586, p = 0.027	+0.265, p = 0.232	
Mechanosensing (cell membrane–associated)	ITGB1	+0.284, p = 0.030	+0.322, p = 0.036	+0.327, p = 0.029	+0.231, p = 0.069	Enhanced expression of membrane-associated mechanosensors involved in integrin-mediated adhesion and mechanosensitive ion channel signaling, indicating increased detection of mechanical stress.
	ITGA7	+0.408, p = 0.035	+0.26, p = 0.21	+0.374, p = 0.06	+0.393, p = 0.041	

(*continued on next page*)

Table 2 (*continued*)

Pathway	Protein	8 h (log_2FC, adj. p)	12 h (log_2FC, adj. p)	24 h (log_2FC, adj. p)	48 h (log_2FC, adj. p)	Functional implication
	PIEZO1	+0.894, p = 0.066	+0.416, p = 0.443	+0.62, p = 0.216	+0.917, p = 0.060	
Mechanotransduction signaling (intracellular)	PTK2	+1.85, p = p < 0.001	−0.336, p = 0.086	−0.62, p = 0.0094	−0.498, p = 0.0098	Upregulation of intracellular mechanotransduction components mediating cytoskeletal tension and focal adhesion signaling, suggesting transmission of mechanical signals to downstream cellular pathways.
	ACTN4	−0.226, p = 0.108	−0.062, p = 0.711	−0.166, p = 0.261	−0.378, p = 0.014	
Mitochondrial dynamics (fission/fusion)	DNM1L	−0.327, p = 0.571	−0.533, p = 0.381	−1.24, p = 0.046	−0.704, p = 0.196	Concurrent upregulation of fission and fusion regulators indicates active restructuring of the mitochondrial network, reflecting adaptive remodeling rather than a shift toward fragmentation or elongation alone.
	MFN1	+1.43, p = 0.00027	+1.49, p = 0.0012	+0.986, p = 0.0094	+0.559, p = 0.046	
	MFN2	+0.124, p = 0.772	+0.308, p = 0.458	+0.319, p = 0.406	+0.114, p = 0.791	
	OPA1	+0.084, p = 0.705	+0.133, p = 0.56	+0.149, p = 0.478	+0.359, p = 0.0744	
Apoptotic signaling (mitochondrial pathway)	BBC3	*0.00, p < 0.001	0.00, p = 1	0.00, p = 1	0.00, p = 1	Concurrent upregulation of pro- and anti-apoptotic regulators indicates induction of apoptosis-related gene expression in response to cellular stress, suggesting a regulated response rather than commitment to irreversible cell death.
	BAX	−0.472, p = 0.458	+0.0258, p = 1	+0.5, p = 0.447	+0.93, p = 0.137	
	CASP3	−4.85, p = 0.0142	−1.44, p = 0.484	−0.239, p = 0.932	−0.133, p = 0.969	
	BCL2	−4.24, p = 0.024	+2.06, p = 0.294	+1.94, p = 0.297	+1.91, p = 0.287	

Values represent log_2 fold change relative to control with Benjamini–Hochberg adjusted p-values. Positive values indicate upregulation, and negative values indicate downregulation. *Proteins with negligible fold changes despite statistical significance are reported but interpreted with caution due to limited effect size. CASP9 was not detected in the proteomics dataset, likely due to its low abundance or limitations in detection sensitivity.

Table 3
Primer sequences for RT-qPCR.

Gene name	Forward primer	Reverse primer	Accession NO.
Mechano-sensing related genes			
Itgb1	TACTGGTCCCGACATCATCC	GGATTTTCACCCGTGTCCCAC	NM_017022.2
Itga7	CCCAGGGCCACGAACAATTT	CTCGTAGGGCCCATCATCCA	NM_001429169.1
Piezo1	GCCTCCCTGTTACGCTTCA	GGCGAGGCATGGTATGTAGG	NM_001434583.1
Actn4	GCCTTTGAGAGTGACCTGGCGG	ATCTTCTGGCACCGTGTGTTGAC	NM_031675.2
Ptk2	ACATCAAGGCGTGTACCTGAGC	GTGAGGATGGTCAAACTGGCGC	NM_013081.2
Mitochondrial dynamics related genes			
Dnm1l	CCAGCTGCCTCAGATTGTCG	GCAGAATAAGAGGTCTCCGGG	NM_001437682.1
Mfn1	TGGTGGCAAACTCGGAATCA	AGCAGAAGCATCCCAACGAT	NM_138976.2
Mfn2	AAGCGCCAGTTTGTGGAGTA	GCTCCAGATTATCCCGGGTG	NM_130894.5
Opa1	AAGACCTCGCCAATTTCGCT	ACAAGAGAAGTGGCTCAGAAGC	NM_001433907.1
Apoptosis related genes			
Casp3	GCTGGACTGCGGTATTGAGA	CTGGATGAACCATGACCCGT	NM_001436900.1
Casp9	CGAACTGCAAGTCGCGGAG	CTTGGCCTGTGTCCTCTAAGC	NM_031632.3
Bbc3	GACCTCAACGCGCAGTACG	GGGAGGAGTCCCATGAAGAGA	NM_173837.2
Bax	GCAGACGGCAACTTCAACTG	GGAAAGGAGGCCATCCCAG	NM_017059.2
Bcl2	CATGTGTGTGGAGAGCGTCA	GCATCCCAGCCTCCGTTATC	NM_016993.2
Pre-mRNA of mitochondrial genes			
Cox6a2	TGAATCTGCTCTCACTCCCAC	AGCAGTTAAGCGAGCAGAGAG	NC_086026.1
Cox5a	CGGACAGGATAGAGCAGTCAC	TTTACGCAACTCCCAGGCAT	NC_086019.1
Reference genes			
Rpl13a	AAAGGTGGTGGTTGTACGCT	GCCTCTTTTGGTCTTGTGCG	NM_173340.2
β-actin	CCCTAAGGCCAACCGTGAA	GAGGCATACAGGGACAACACA	NM_031144.3

Within Complex IV, both *Cox6a2* and *Cox5a* transcripts were significantly upregulated after 8 h of vibration (2.92-fold, $p < 0.001$, and 1.49-fold, $p < 0.01$, respectively) (Fig. 3A and C). Notably, as mentioned before, the COX6A2 protein was not detected in the proteomics dataset, likely due to its low abundance. By comparison, *Cox6c* transcript expression remained stable across all timepoints, with no significant changes observed, suggesting that not all Complex IV subunits are equally responsive at the transcriptional level under vibration. To assess whether transcriptional upregulation was accompanied by impaired RNA processing, we quantified unspliced pre-mRNA levels of both *Cox5a* and *Cox6a2,* which displayed an increasing trend following vibration exposure, with *Cox5a* showing significant accumulation at 48 h (1.83-fold, $p < 0.05$) (Fig. 3B and D). These findings, together with the proteomic downregulation of spliceosome-associated factors such as SRSF2, DDX46, and SUB1, indicate that increased transcription is accompanied by reduced RNA processing efficiency at later time points. In Complex I, *Ndufs4* showed a mild upward trend at later time points, consistent with the proteomic observation of selective subunit upregulation. This suggests that the muscle cell may be stabilizing or accumulating NDUFS4 protein, even though the mRNA increase is modest, supporting the view of subunit-specific remodeling rather than uniform Complex I activation.

The expression levels of genes involved in upstream mechanosensory components at the cell membrane were significantly increased after 8 h of vibration. Significant values were observed for *Itgb1* (1.31-fold, $p < 0.05$) and *Itga7* (1.73-fold, $p < 0.001$), which mediate integrin-

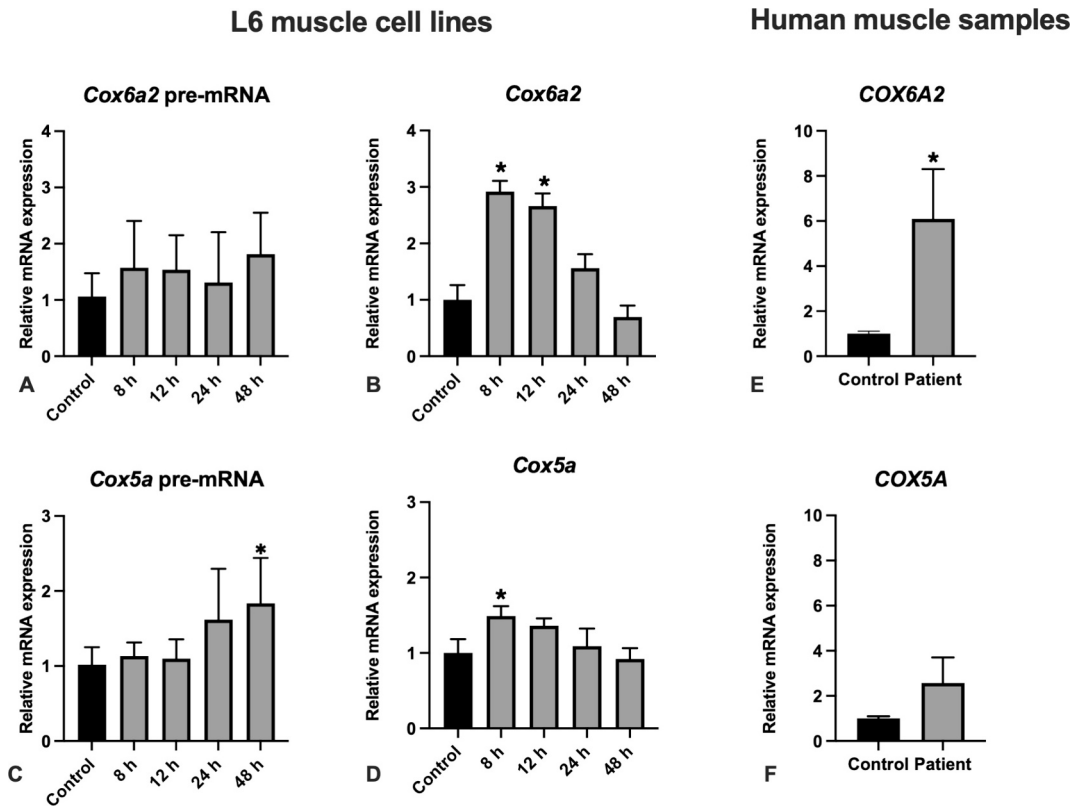


Fig. 3. Complex IV (COX) transcript expression in L6 muscle cells and human upper airway muscle biopsies. Relative unspliced pre-mRNA levels of *Cox6a2* (A) and *Cox5a* (C), and corresponding mRNA expression of *Cox6a2* (B) and *Cox5a* (D) in L6 muscle cells following snoring-induced vibration exposure. Both *Cox6a2* and *Cox5a* mRNA levels were significantly upregulated at early time points (8 and 12 h and 8 h, respectively), whereas pre-mRNA levels showed an increasing trend, with *Cox5a* pre-mRNA significantly elevated at 48 h. Relative mRNA expression of COX6A2 (E) and COX5A (F) in human upper airway muscle biopsies from snorers and OSA patients compared with controls. *COX6A2* expression was significantly increased in patient samples, whereas *COX5A* showed a non-significant upward trend. Data are presented as mean ± SD. *p < 0.05 compared with control.

dependent adhesion, and *Piezo1* (1.77-fold, $p < 0.05$), a mechanosensitive ion channel. These transcriptional changes are consistent with the proteomic upregulation of integrin subunits ITGB1 and ITGA7, as well as a similar increasing for PIEZO1 protein levels, supporting activation of upstream mechanosensory pathways. Similarly, intracellular downstream mechanotransduction signaling components *Actn4* (1.85-fold, $p < 0.05$) *and Ptk2* (1.54-fold, $p < 0.05$) were upregulated after 8 h of vibration, and showed an upward trend at 24 and 48 h. Consistent with this, proteomic analysis revealed a significantly marked increase in PTK2 abundance at 8 h, followed by a significant reduction at 24 h and 48 h, indicating early activation of focal adhesion signaling followed by attenuation at later time points (Fig. 4).

The mitochondrial fission gene *Dnm1l* and fusion-related genes *Mfn1* (mitofusin 1) and *Opa1* were significantly upregulated after 8 h of vibration (1.49, 1.37, and 1.29-fold, respectively, $p < 0.05$). This transcriptional activation of both fission and fusion regulators contrasts with the proteomic profile, where DNM1L protein levels were reduced, and MFN1 was significantly increased across all time points, suggesting differential regulation at the transcriptional and protein levels. At later time points, a mild upward trend was observed in gene expression for *Opa1*, however, a significant increase was only detected at 24 h (1.88-fold, $p < 0.05$). *Mfn2* did not show significant changes. Together, these findings indicate an active complex remodeling of mitochondrial dynamics, with a shift toward fusion at the protein level despite early transcriptional activation of both processes (Fig. 5).

The expression of the mitochondrial pro-apoptotic genes *Bbc3* (activator of mitochondrial apoptosis) and *Bax* (mediator of mitochondrial membrane permeabilization) was significantly increased at all time points. *Bbc3* expression increased progressively from 2.03-fold at 8 h ($p < 0.05$) to 4.74-fold at 48 h ($p < 0.01$). Similarly, *Bax* expression increased from 1.26-fold at 8 h ($p < 0.05$) to 2.46-fold at 48 h ($p < 0.05$). However, these transcriptional changes were not accompanied by parallel proteomic changes, with minimal changes in BBC3 protein levels. BAX protein levels remained largely unaltered (see Table 2). Expression of the pro-apoptotic genes *Casp3* and *Casp9* increased over time. Executioner Casp3 was significantly upregulated at 24 h (1.59-fold, $p < 0.05$), whereas initiator *Casp9* showed significant increases at 8 and 48 h (1.52- and 1.95-fold, respectively; $p < 0.05$). In contrast, proteomic analysis showed a significant decrease in CASP3 protein abundance at 8 h and no detection of CASP9, suggesting limited translation into functional apoptotic execution. The mitochondrial anti-apoptotic regulator *Bcl2* gene was significantly upregulated at 8 h (1.66-fold, $p < 0.01$), 24 h (1.56-fold, $p < 0.05$), and 48 h (2.71-fold, $p < 0.05$). Proteomic data showed a significant reduction at 8 h in BCL2 protein levels, followed by a tendency toward recovery (Fig. 6, table 2). Taken together, the combined transcriptomic and proteomic data suggest activation of stress-responsive apoptotic signaling without evidence of irreversible cell death.

3.1.13. *Cellular senescence β-galactosidase staining*

After 8 h of vibration, a modest but non-significant increase in senescent cells was observed. At 12 h, there was a significant increase ($p < 0.05$) in senescent cells (mean 15.3 ± SD 6.22%) compared with controls (mean 6.75 ± SD 1.84%). At 24 h, the proportion of senescent cells decreased toward control levels, suggesting a partial recovery or adaptation (Fig. 7). Notably, the increase in senescence coincided with the transcriptional upregulation of apoptosis-related genes *Bbc3, Bax, Casp3,* and *Casp9*, but this increase was not reflected at the protein level.

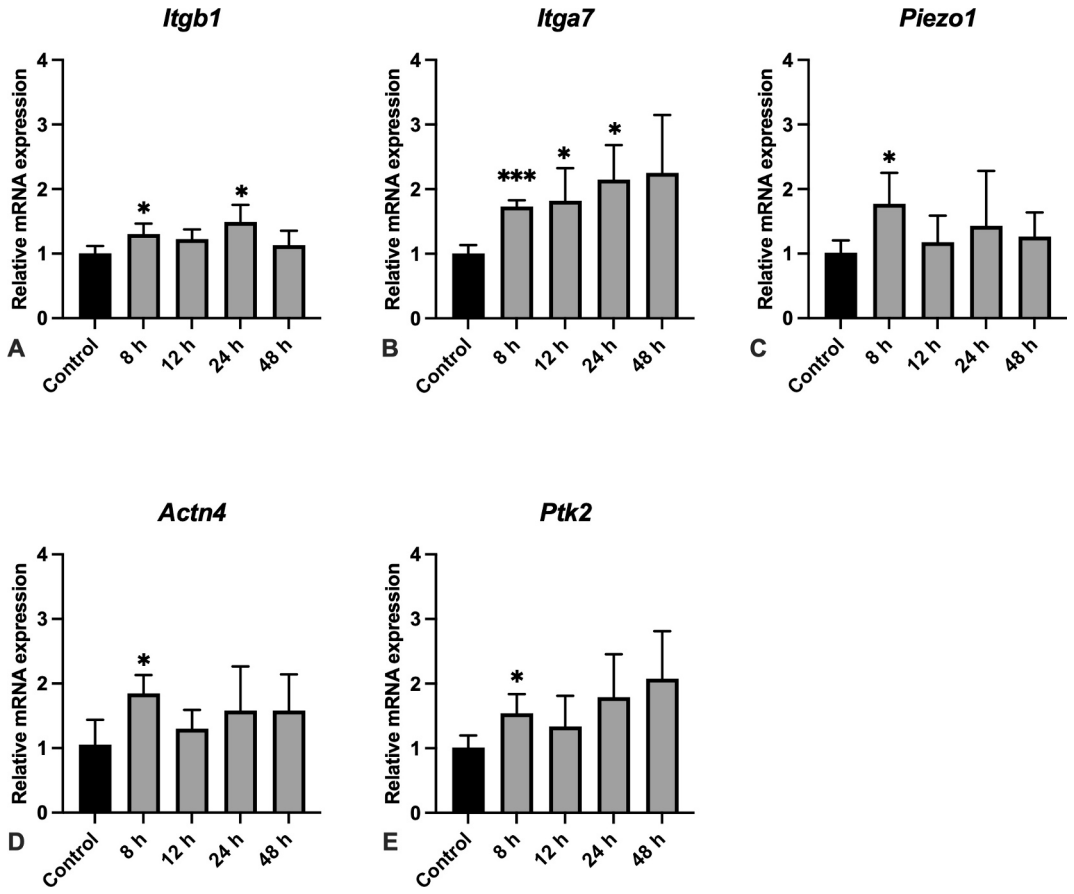


Fig. 4. Activation of mechanosensing and mechanotransduction signaling in L6 muscle cells following vibration exposure. Relative mRNA expression of mechanosensory genes *Itgb1* (A), *Itga7* (B), and *Piezo1* (C), and mechanotransduction-associated genes Actn4 (D) and *Ptk2* (E) in L6 muscle cells exposed to snoring-induced vibration. Expression of all genes was significantly increased at 8 h, indicating early activation of membrane-associated mechanosensors and downstream intracellular signaling components. Integrin subunits (*Itgb1, Itga7*) and the mechanosensitive ion channel (*Piezo1*) represent key upstream sensors, whereas *Actn4* and *Ptk2* reflect cytoskeletal remodeling and focal adhesion signaling. At later time points, an overall upward trend was observed, with statistically significant increases persisting for *Itgb1* (24 h) and *Itga7* (12 and 24 h). Data are presented as mean ± SD. *p < 0.05, **p < 0.01, ***p < 0.001 compared with control.

3.1.14. Rates of aerobic respiration and glycolysis following vibration experiments

Mitochondrial respiration and glycolytic activity were evaluated using the Seahorse XFp Mito Stress Test, measuring oxygen consumption rate (OCR) and extracellular acidification rate (ECAR), respectively. Since proteomic analyses identified distinct mitochondrial remodeling in L6 muscle cells following snoring-induced vibration at early (8 h) and late (48 h) time points, these time points were selected for functional assessment.

After 8 h of vibration exposure, OCR exhibited a near-complete collapse across all assay parameters, including basal respiration, maximal respiration, ATP-linked respiration, proton leak, and non-mitochondrial oxygen consumption ($p < 0.0001$; Fig. 8A, C–G), indicating severe mitochondrial dysfunction. In contrast, after 48 h of vibration exposure, OCR parameters recovered to levels that were not statistically different from those of controls (Fig. 8A, C–G), despite persistent abnormalities in proteomic and RNA-processing pathways.

While basal ECAR values were comparable between control, 8 h, and 48 h conditions, cells exposed to vibration for 8 h failed to increase ECAR following ATP synthase inhibition by oligomycin, indicating a profound loss of glycolytic reserve ($p < 0.0001$; Fig. 8B). Although ECAR responsiveness partially recovered after 48 h of vibration, the glycolytic response remained blunted compared to controls, suggesting incomplete restoration of glycolytic flexibility. This impaired ECAR response is consistent with proteomic evidence of coordinated downregulation of multiple glycolytic enzymes and regulatory proteins, indicating a reduced capacity to rapidly upregulate glycolysis in response to energetic stress.

Although mitochondrial oxygen consumption returned to control levels after 48 h of vibration exposure, the inability of cells to appropriately increase glycolysis in response to mitochondrial ATP synthase inhibition indicates that functional coupling between mitochondrial respiration and glycolytic compensation remains impaired, consistent with the downregulation of key glycolytic enzymes observed in the proteomic analysis.

3.2. Human muscle samples

3.2.1. Immunohistochemical abnormalities in mitochondrial activity and organization

Immunohistochemical analysis of biopsies from all patients revealed a significant number of fibers with abnormal intra-myofibrillar mitochondrial distribution as shown by Tomm 20 staining, and reduced COX2 and COX4 activity (36.9 ± 19.7%, Fig. 9B-F), whereas no fibers with these abnormalities were observed in controls (Fig. 9A). A common abnormal staining pattern observed with all three mAbs was the replacement of the typical mitochondrial lattice pattern with irregular trabecular septations, areas devoid of staining, and subsarcolemmal accumulation of mitochondria in a ring-like pattern (Fig. 9B-F). Small, round-shaped fibers with absent or very low mitochondrial activity in the center but high subsarcolemmal activity were also common (Fig. 9B).

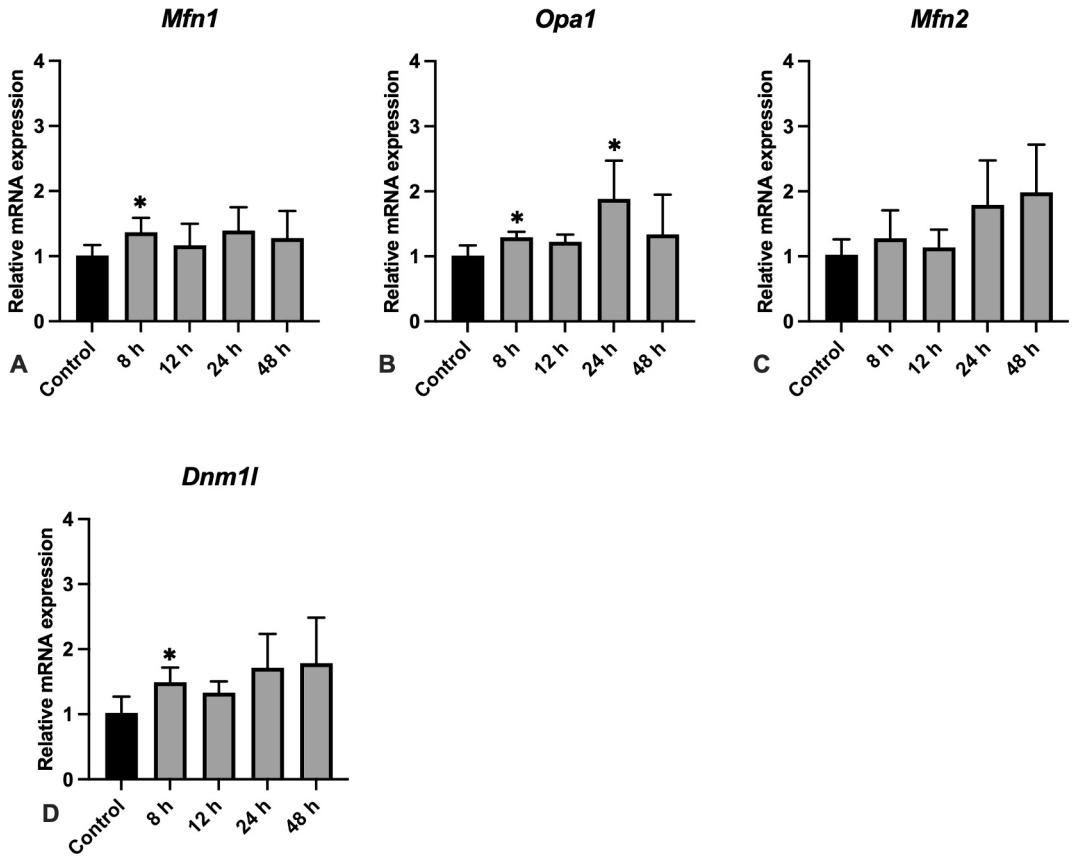


Fig. 5. Regulation of mitochondrial dynamics in L6 muscle cells following vibration exposure. Relative mRNA expression of mitochondrial fusion-related genes *Mfn1* (A), *Mfn2* (B), and *Opa1* (C), and the mitochondrial fission gene *Dnm1l* (D) in L6 muscle cells exposed to snoring-induced vibration. Expression of *Dnm1l, Mfn1*, and *Opa*1 was significantly increased at 8 h, indicating early activation of mitochondrial dynamics in response to mechanical stress. At later time points, a mild upward trend was observed, with a statistically significant increase detected only for *Opa1* at 24 h, while *Mfn2* showed no significant changes. These transcriptional changes are consistent with dynamic remodeling of the mitochondria, involving both fission and fusion processes. Data are presented as mean ± SD. *$p < 0.05$ compared with control.

3.2.2. *Enzyme-histochemical SDH and COX activity*

In most patient muscle samples, fibers were observed that were stained for SDH but not for COX, the terminal enzyme of the mitochondrial respiratory chain that drives ATP synthesis (Fig. 9E-F).

3.2.3. *Muscle fiber cross-sectional area and variability in fiber size*

In patients, muscle fibers had a mean fCSA similar to that in controls (1153 $\mu m^2 \pm 629$ vs. 1170 $\mu m^2 \pm 221$); however, fiber size variability (CV) was significantly higher in patients than in controls (66.5% vs. 49.3%, $p = 0.005$). The highest CV was observed in fibers with a disorganized mitochondrial distribution (79.8%) or nearly absent mitochondrial activity (55.7%) (Fig. 9B-F).

3.2.4. *Muscle fiber capillarization*

The number of capillaries supplying each muscle fiber (CAF) was significantly lower in patients than in controls (0.6 ± 0.26 vs. 1.29 ± 0.31, $p = 0.013$). When fibers in patients were divided based on mitochondrial distribution and staining activity, the CAF value was significantly lower in fibers lacking mitochondrial activity (0.52 ± 0.25, $p = 0.001$) or showing mitochondrial disorganization (0.48 ± 0.24, $p = 0.001$) than in fibers with a normal staining pattern (0.66 ± 0.28) (Fig. 9A-D).

In patients, the number of capillaries around fibers in relation to fiber area (CAFA) was significantly lower ($p < 0.01$) in fibers with disorganized mitochondrial distribution (0.63 ± 0.42), fibers with weak (0.55 ± 0.32) or no mitochondrial activity (0.52 ± 0.40) than in fibers with a normal appearance (0.78 ± 0.46) and in those in the control group (1.34 ± 0.50) (Fig. 9A-D).

3.2.5. *Mitochondrial gene expression in human biopsies*

Since *COX5A* and *COX6A2*, both encoding subunits of mitochondrial Complex IV, were significantly upregulated in L6 muscle cells exposed to the in vitro vibration model, they were selected for investigation in patient muscle biopsies. The expression of *COX5A* mRNA was upregulated 2.5-fold ($p = 0.059$) in patients, and COX6A mRNA displayed a significant 6-fold ($p = 0.008$) upregulation (Fig. 3E and F).

4. Discussion

This study demonstrates for the first time that snoring-induced vibrations disrupt mitochondrial homeostasis in muscle cells. Consistent abnormalities in mitochondrial organization and COX activity were observed in human upper airway muscle biopsies from snorers and OSA patients. The experimental in vitro model revealed selective changes in oxidative phosphorylation in Complexes I, IV, and V of the electron transport chain (ETC) in muscle cells. Importantly, vibration exposure affected not only mitochondrial respiratory chain components but also the glycolytic machinery, which normally acts as a compensatory energy pathway during mitochondrial stress. Furthermore, our transcriptomic

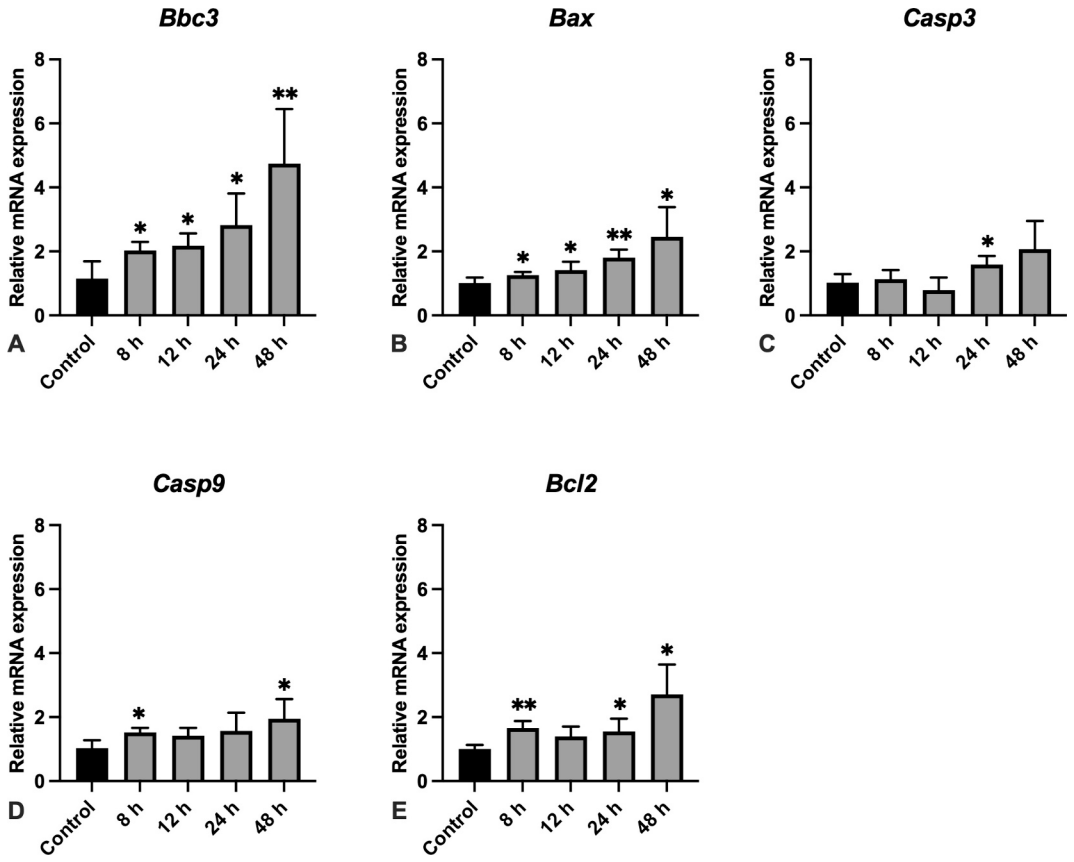


Fig. 6. Regulation of apoptosis-related gene expression in L6 muscle cells following vibration exposure. Relative mRNA expression of pro-apoptotic genes *Bbc3* (A), *Bax* (B), *Casp3* (C), and *Casp9* (D), and the anti-apoptotic gene *Bcl2* (E) in L6 muscle cells exposed to snoring-induced vibration. Expression of *Bbc3* and *Bax* was significantly increased across all time points, while *Casp3* and *Casp9* showed significant upregulation at selected time points, indicating activation of apoptosis-related signaling pathways. The anti-apoptotic gene *Bcl2* was also significantly upregulated, suggesting a concurrent protective response. Together, these transcriptional changes indicate activation of cellular stress and apoptotic signaling rather than a clear shift toward irreversible cell death. Data are presented as mean ± SD. *$p < 0.05$, **$p < 0.01$ compared with control.

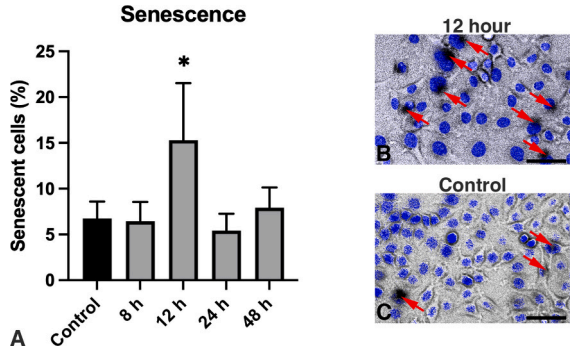


Fig. 7. Transient induction of cellular senescence following snoring-induced mechanical stress. Cellular senescence was assessed by β-galactosidase staining at different time points (8–24 h) following exposure to snoring vibrations. The percentage of senescent cells was quantified relative to the total cell number (A). A significant increase in senescent cells was observed at 12 h compared to the control. Senescence levels decreased at later time points (24 h and 48 h). Data are presented as mean ± SD (n = 4). *$p < 0.05$ vs control. Images of L6 cells at 12 h (B) and control (C) show β-galactosidase–positive cells (black staining, red arrows). Nuclei are counterstained with DAPI (blue). Scale bar 50 μm. (For interpretation of the references to colour in this figure legend, the reader is referred to the web version of this article.)

and proteomic data link mechanical stimuli to mitochondrial remodeling by showing activation of upstream mechanosensing components, including integrins and PIEZO1, as well as downstream mechanotransduction signaling. The vibrations also triggered imbalances in RNA-processing factors, mitochondrial transporters, and compartment-specific chaperone systems, indicating disruption of mitochondrial proteostasis. This interpretation was further supported by the accumulation of unspliced pre-mRNA, indicating impaired RNA maturation despite transcriptional upregulation. These molecular disturbances coincided with a marked collapse in mitochondrial respiration and glycolytic reserve after 8 h of snoring-induced vibrations. Together, our findings demonstrate that snoring-induced vibration elicits a

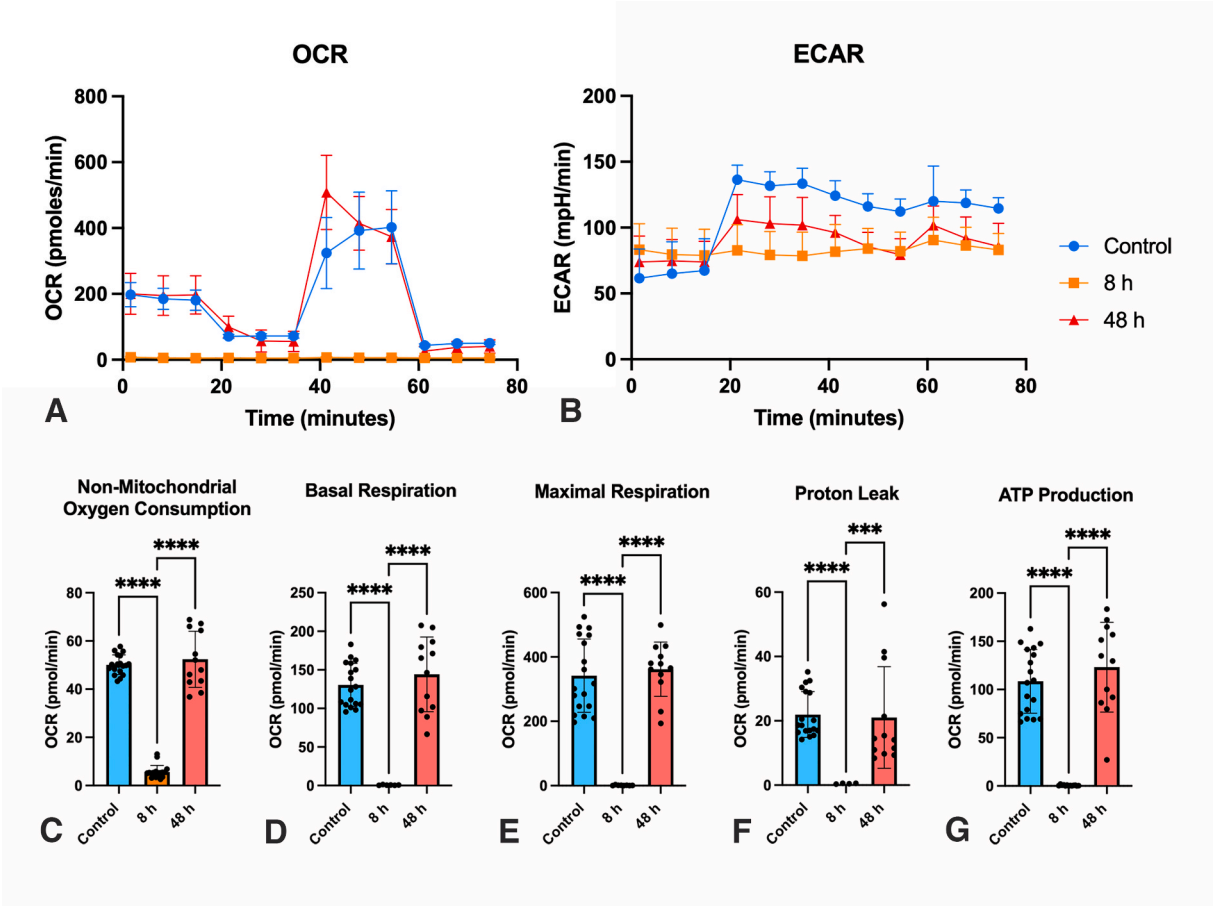


Fig. 8. Real-time bioenergetic responses to snoring-induced vibration in L6 myoblasts. (A) Oxygen consumption rate (OCR) profiles show a near-complete collapse of mitochondrial respiration after 8 hours of vibration, whereas cells exposed for 48 hours display OCR values comparable to controls. (B) Extracellular acidification rate (ECAR) analysis demonstrates reduced glycolytic activity and loss of glycolytic reserve at 8 hours, with failure to increase ECAR following oligomycin injection, while control and 48-hour vibrated cells retain glycolytic responsiveness. (C–G) Quantification of non-mitochondrial oxygen consumption, basal respiration, maximal respiration, proton leak, and ATP-linked respiration reveals severe suppression of all mitochondrial parameters at 8 hours, with recovery to control levels at 48 hours. Data are presented as mean ± SEM. ****$p < 0.0001$ compared with control.

transcriptional stress response in muscle cells that fails at the level of protein processing and respiratory complex assembly, resulting in transcript–protein uncoupling, impaired adaptive energy metabolism, likely leading to muscle weakness.

4.1. *Snoring-induced vibration disrupts OXPHOS protein assembly*

Across the mitochondrial proteome, experimental vibration exposure induced pronounced subunit-specific remodeling of the respiratory chain in L6 muscle cells. Multiple components of Complexes I, IV, and V increased in abundance over time, indicating an active response to vibration stress. Notably, several Complex IV subunits were unchanged or showed upregulation after 8 h of vibration, whereas Complex I and Complex V subunits were upregulated at later time points. Within Complex I, delayed accumulation of NDUFS subunits at 24 and 48 h may therefore reflect the persistence of improperly assembled or functionally compromised complexes, rather than successful restoration of NADH-oxidizing capacity. Similarly, increased abundance of both F_0 and F_1 subunits of ATP synthase reflects accumulation of individual components that may not be accompanied by fully coordinated assembly into intact ATP synthase holoenzymes (Walker, 2013). Overall, these findings indicate increased abundance of selected OXPHOS subunits across respiratory complexes, although not all may be functionally active. Accumulation of non-functional proteins in complex 1 has been experimentally demonstrated in patient-derived cells (Guerrero-Castillo et al., 2017).

4.2. *Mechanosensing–mechanotransduction axis in mitochondrial remodeling triggered by snoring-induced vibration*

To better understand the upstream mechanisms linking mechanical vibration to mitochondrial dysfunction, we integrated transcriptomic and proteomic analyses of mechanosensory and mechanotransduction components. Vibration exposure induced early upregulation of membrane-associated mechanosensor gene expression, including integrin subunits (*Itgb1, Itga7*) and the mechanosensitive ion channel *Piezo1* (Fig. 4), accompanied by corresponding increases or upward trends at the protein level (Table 2). These findings indicate enhanced detection of mechanical stress at the cell membrane through integrin-mediated adhesion and ion channel activation. This is consistent with the established role of integrins as primary mechanosensors that transmit extracellular forces into intracellular signaling pathways (Hynes, 2002; Sun et al., 2016), and with PIEZO1 functioning as a mechanically activated ion channel mediating cellular responses to mechanical stimuli (Coste et al., 2010; Syeda et al., 2016).

Downstream mechanotransduction signaling was characterized by early activation of focal adhesion pathways, reflected by increased *Ptk2* gene expression and PTK2 protein abundance, followed by attenuation at the protein level despite sustained transcriptional elevation, indicating temporal decoupling between gene expression and protein regulation. This pattern is consistent with the established role of PTK2 as a rapidly activated mediator of integrin-dependent mechanotransduction signaling (Mitra et al., 2005; Geiger et al., 2009). In

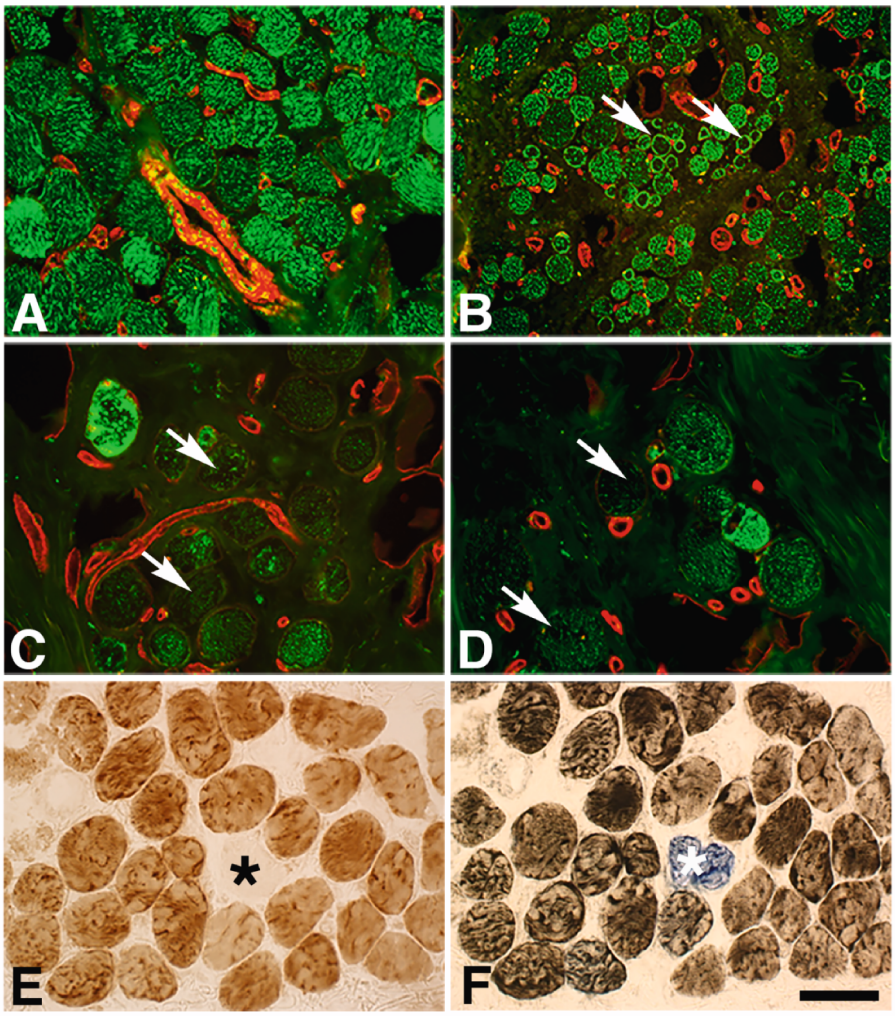


Fig. 9. Mitochondrial organization, oxidative activity, and capillarization in upper airway muscle biopsies from controls and patients. Representative muscle cross-sections immunostained for COX subunit 2 (green) and capillaries (red) from a control subject (A) and patients with obstructive sleep apnea (B–F). Control muscle fibers show a normal lattice-like intramyofibrillar distribution of mitochondrial COX 2 activity (A). In contrast, patient muscle fibers exhibit marked abnormalities in mitochondrial organization and oxidative activity, including irregular trabecular septations, areas of reduced or absent COX 2 staining, and subsarcolemmal accumulation of mitochondria (B–D, arrows). Small, rounded fibers with low or absence of central mitochondrial activity but increased subsarcolemmal staining are shown in B (arrows). Note the low capillary supply of fibers with disrupted mitochondrial distribution or reduced oxidative activity in C and D. Muscle sections stained for COX (brown, E) and double-stained for COX and SDH (blue, F). Cox negative fibers (blue) are marked with asterisks. Scale bar 40μm.

contrast, while *Actn4* gene expression was increased, corresponding changes in ACTN4 protein levels were modest, suggesting post-transcriptional regulation or differences in protein turnover. Such divergence between mRNA and protein abundance is a well-recognized feature of cellular stress responses and complex regulatory systems (Vogel and Marcotte, 2012), and may also reflect the role of cytoskeletal networks in dynamically transmitting and adapting to mechanical forces (Ingber, 2006). Together, these findings support a model in which mechanical stimulation induces a rapid mechanotransduction response, characterized by early transcriptomic activation followed by target-dependent protein-level changes. Some components (e.g., PTK2 and integrins) showed corresponding increases, whereas others such as ACTN4 exhibited only modest protein-level changes despite transcriptional upregulation (Fig. 4), thereby driving cytoskeletal remodeling and mitochondrial adaptation, potentially promoting cellular survival rather than immediate cell death.

4.3. Mitochondrial dynamics and transcript–protein decoupling under snoring-induced vibration

At the mitochondrial level, transcriptional upregulation of both fission and fusion regulators (*Dnm1l, Mfn1, Opa1*) contrasted with proteomic data showing reduced DNM1L and increased MFN1, indicating a shift toward fusion-dominated remodeling at the protein level. This imbalance suggests a reorganization of the mitochondrial network toward a more fused and interconnected state. This pattern aligns with the established role of mitochondrial dynamics as a balance between fission and fusion processes that are tightly regulated under stress conditions (Youle and van der Bliek, 2012). The divergence between transcript and protein levels suggests post-transcriptional regulation of mitochondrial dynamics, a phenomenon commonly observed in cellular stress responses where protein abundance does not directly mirror mRNA expression (Vogel and Marcotte, 2012). Such fusion-dominated

restructuring is a well-established adaptive response that helps preserve mitochondrial function, maintain cristae integrity, and sustain energy production under stressful conditions (Liesa and Shirihai, 2013). Our findings are consistent with adaptive restructuring of the mitochondrial network towards a more fused and interconnected state in response to mechanical stress (Fig. 5).

4.4. Activation of apoptotic signaling without evidence of cell death

Despite upregulation of apoptosis-related genes (*Casp3, Casp9, Bbc3, Bax*), corresponding protein-level changes were inconsistent, with key apoptotic effectors unchanged or undetected (Table 2). This divergence between transcript and protein levels is consistent with the well-established decoupling of mRNA and protein abundance in complex cellular responses (Vogel and Marcotte, 2012). Importantly, gene activation alone is insufficient to drive apoptosis, which requires coordinated protein-level events such as mitochondrial outer membrane permeabilization and caspase activation (Tait and Green, 2010). Accordingly, the observed pattern is more consistent with apoptotic priming or stress signaling rather than commitment to cell death (Galluzzi et al., 2018). This is further supported by β-galactosidase staining, which revealed a transient increase in senescent cells, peaking at 12 h. Together, these findings indicate that vibration triggers a mechano-responsive axis linking membrane sensing, mitochondrial remodeling, and cellular stress signaling, consistent with an adaptive response rather than progression to cell death. (Figs. 6 and 7).

4.5. Impaired glycolytic reserve limits metabolic flexibility

Despite the increased abundance of selected OXPHOS subunits, vibration exposure was accompanied by downregulation of key glycolytic enzymes. Proteomic analysis revealed suppression of the rate-limiting glycolytic enzyme PFKL along with downregulation of multiple downstream glycolytic enzymes. This pattern is expected to constrain maximal glycolytic flux rather than basal glycolytic activity, because downregulation of the rate-limiting PFK-1 step restricts stress-induced upregulation of glycolysis despite preservation of downstream pathway components (Mor et al., 2011). Consequently, this pattern is expected to limit the capacity for adaptive increases in glycolytic ATP production under conditions of energetic stress.

4.6. Altered mitochondrial transport and proteostasis

An efficient mitochondrial energy metabolism requires coordinated transport of substrates and nucleotides across the inner mitochondrial membrane (Kunji et al., 2020). Vibration exposure suppressed mitochondrial amino acid transport at early time points (8–12 h), likely constraining anaplerotic input into the tricarboxylic acid cycle and contributing to the initial collapse of mitochondrial respiration. In contrast, transient upregulation of the adenine nucleotide translocator at 12 h suggests prioritization of ADP/ATP to adjust nucleotide exchange despite impaired upstream respiratory efficiency (Kunji et al., 2016).

In parallel, vibration induced compartment-specific alterations in protein quality-control systems (Voos, 2013). Mitochondrial chaperones involved in protein import and folding, HSPE1, were consistently upregulated across all time points, whereas HSPA9 showed transient upregulation between 8 and 24 h, consistent with increased engagement of mitochondrial proteostasis mechanisms under stress. Conversely, cytosolic chaperone HSP90 isoforms were downregulated across all time points, indicating redistribution of proteostatic resources toward mitochondrial maintenance rather than a generalized stress response. This targeted but imbalanced proteostatic response may be insufficient to ensure coordinated assembly and stabilization of mitochondrial respiratory complexes during prolonged vibration exposure.

4.7. Alterations in RNA-processing, splicing, and ribosomal proteins

Accurate RNA processing is essential for coordinated synthesis and assembly of nuclear-encoded mitochondrial proteins. Snoring-induced vibration dysregulated components of the RNA-processing and splicing apparatus, most prominently through downregulation of spliceosome-associated factors such as serine/arginine-rich splicing factor 2 (SRSF2) and DEAD-box helicase 46 (DDX46), which were consistently reduced across time points. These factors are critical for splicing fidelity and efficiency (Wilkinson et al., 2020; Zhou and Fu, 2013), and their suppression is expected to impair RNA maturation, increasing the likelihood of aberrant transcripts with downstream consequences for protein stability and assembly. In addition, SUB1, which links transcription to RNA processing, showed significant downregulation from 8–24 h. In contrast, the core spliceosomal component SNRPC exhibited modest upregulation across multiple time points, highlighting heterogeneous regulation within the RNA-processing machinery rather than uniform suppression or compensation.

Snoring-induced vibrations also affected components of the mitochondrial translation machinery. Two mitochondrial ribosomal proteins, MRPL22 and MRPL37, were upregulated from 8 to 24 h, indicating a transient increase in mitochondrial protein synthesis in response to vibration stress. Mitochondrial ribosomes are essential for synthesizing respiratory chain subunits, and transient changes in MRPL abundance are often interpreted as adaptive attempts to sustain mitochondrial protein production under stress (Wang et al., 2021). This is further supported by the accumulation of unspliced pre-mRNA for mitochondrial transcripts, indicating reduced RNA-processing efficiency despite transcriptional upregulation. The accumulation of precursor transcripts is a well-established consequence of impaired spliceosome function (Wahl et al., 2009), and cellular stress has been shown to disrupt RNA splicing and processing efficiency (Dvinge et al., 2019). Together, these findings indicate an imbalance in post-transcriptional regulation spanning RNA processing, splicing, and mitochondrial translation, which likely constrains the efficient production of mature transcripts and the coordinated assembly of mitochondrial respiratory complexes.

4.8. Transcript–protein dissociation during vibration-induced mitochondrial stress

Despite evidence of transcriptional activation, mitochondrial protein abundance did not consistently reflect corresponding changes at the transcript level, indicating a decoupling between gene expression and protein regulation. To further examine this, we analyzed transcript levels of selected mitochondrial subunits in L6 muscle cells following snoring-induced vibration. Transcriptomic analysis revealed selective upregulation of nuclear-encoded mitochondrial transcripts. Within Complex IV, transcripts encoding *Cox5a* and *Cox6a2* were significantly upregulated at early time points, whereas other subunits, such as *Cox6c,* were unchanged, indicating subunit-specific transcriptional activation. Importantly, this transcriptional upregulation was accompanied by an accumulation of unspliced pre-mRNA, indicating reduced RNA processing efficiency. This is consistent with impaired spliceosome function, which is required for the conversion of pre-mRNA into fully processed mature transcripts (Scotti and Swanson, 2016), and aligns with the observed downregulation of spliceosome-associated factors described above. For Complex I, modest increases in *Ndufs4* transcripts occurred despite clear accumulation of NDUFS4 protein, supporting post-transcriptional stabilization or altered turnover rather than strong transcriptional induction. Similar transcript–protein dissociation has been described during Complex I assembly and repair, in which subunits accumulate as stable assembly intermediates without proportional transcriptional upregulation (Guerrero-Castillo et al., 2017). Our findings are consistent with this concept and show that vibration-induced disruption of RNA processing, together with downstream post-translational processing and assembly of mitochondrial proteins, alters

the organization of mitochondrial respiratory complexes.

4.9. Real-time assessment of mitochondrial and glycolytic function

Real-time bioenergetic analysis demonstrated the functional consequences of vibration-induced molecular disturbances in L6 muscle cells. After 8 h of vibration exposure, muscle cells exhibited a near-complete collapse of mitochondrial oxygen consumption, affecting basal, maximal, and ATP-linked respiration, together with a marked loss of glycolytic reserve (Fig. 8). This acute bioenergetic failure occurred despite transcriptional upregulation of selected nuclear-encoded mitochondrial genes, as discussed above, indicating that early transcriptional activation alone is insufficient to sustain mitochondrial function.

By 48 h, basal mitochondrial respiration recovered to levels comparable to controls, coinciding with increased abundance of selected respiratory chain subunits. However, this apparent recovery remained incomplete, as cells at this time point were still unable to increase glycolytic flux in response to mitochondrial ATP synthase inhibition, indicating persistent impairment of energy metabolism (Fig. 8). Thus, upregulation of individual respiratory subunits does not necessarily reflect restoration of fully functional holoenzymes or effective metabolic flexibility.

4.10. Relevance to upper-airway muscle pathology in snorers and OSA

The in vitro findings are in line with observations in human upper-airway muscle biopsies from snoring and OSA patients. Immuno- and enzyme-histochemical analyses revealed muscle fibers with pronounced mitochondrial disorganization, reduced or absent COX activity, and decreased capillary supply, consistent with a decreased capacity for oxidative synthesis of ATP (Stål and Johansson, 2012). Reduced blood supply to muscle fibers may further constrain oxygen delivery, reinforcing a cycle of impaired energy metabolism and structural instability. These observations align with our previous reports linking snoring and OSA to abnormalities in the mitochondrial and capillary compartments, as well as dysregulation of the cytoskeletal protein desmin in upper-airway muscles (Shah et al., 2018, 2019a,b; Stål et al., 2024; Stål and Johansson, 2012). Given desmin's critical role in maintaining myofibrillar integrity and mitochondrial positioning, its dysregulation may contribute to the observed mitochondrial disorganization, (Clemen et al., 2013; Smolina et al., 2020; Agnetti et al., 2022). Furthermore, mitochondrial gene expression analysis revealed upregulation of selected nuclear-encoded Complex IV transcripts *COX5A* and *COX6A2*, similar to that observed in vibrated L6 muscle cells (Fig. 3). However, in L6 cells this response was transient and most pronounced at early time points, likely reflecting the proliferative and adaptive nature of L6 myoblasts, which can normalize transcriptional responses over time, in contrast to terminally differentiated muscle fibers in vivo. In human muscle biopsies, the sustained upregulation likely reflects a compensatory response to chronic mechanical stress induced by long-term exposure to snoring-induced vibrations. This transcriptional response suggests a compensatory attempt to sustain oxidative capacity in damaged fibers. However, persistent mitochondrial disorganization and reduced COX activity indicate that transcriptional activation alone is insufficient to restore functional mitochondrial function in patients.

5. Study limitations

The experimental model using L6 myoblasts does not fully replicate the effect of vibrations on the upper airway muscles in vivo. Moreover, the long-term effects of vibrations, as experienced in snoring and OSA patients, were not analyzed. The model also does not account for interindividual variability in snoring vibration patterns. Despite these considerations, the consistency across transcriptomic, proteomic, and human data supports the biological relevance of the model. Moreover, protein expression of COX5A and COX6A2 was not directly assessed in the human upper airway muscle biopsies due to limited tissue availability. Future studies integrating transcriptomic, proteomic, and functional analyses in patient tissue are therefore needed to further clarify the relationship between transcriptional activation and mitochondrial dysfunction in response to snoring-induced vibrations.

6. Conclusion

This study identifies snoring-induced vibration as an unrecognized mechanical stressor disrupting mitochondrial homeostasis in muscle cells. The in vitro model demonstrates activation of upstream mechanosensing components and downstream mechanotransduction signaling, linking membrane-level force detection to mitochondrial remodeling. Moreover, vibration impairs mitochondrial function by disrupting RNA processing, protein synthesis, and respiratory complex assembly, resulting in decoupling between transcript and protein expression. In addition, vibration impairs compensatory glycolytic adaptation, thereby reducing metabolic flexibility under stress despite partial recovery of mitochondrial respiration. These findings align with mitochondrial and cellular oxygenation abnormalities in the upper airway of snoring and OSA patients. Our findings provide a mechanistic framework linking snoring-related vibrations to disturbances in energy metabolism, integrating mechanotransduction signaling with post-transcriptional dysregulation. Together, these processes likely contribute to muscle weakness and increased susceptibility to upper airway dysfunction. Given the prevalence of occupational vibration injuries, these findings also contribute to a broader understanding of the biological effects of vibration on muscles.

CRediT authorship contribution statement

Per Stål: Writing – review & editing, Writing – original draft, Visualization, Validation, Software, Resources, Methodology, Investigation, Funding acquisition, Formal analysis, Data curation, Conceptualization. **Roine El-Habta:** Writing – review & editing, Visualization, Investigation, Formal analysis, Data curation. **Yu-Cheng Qian:** Writing – review & editing, Investigation. **Shaochun Zhu:** Writing – review & editing, Software, Resources, Data curation. **Chloe Williams:** Writing – review & editing, Visualization, Investigation, Data curation. **André Mateus:** Writing – review & editing, Software, Resources, Funding acquisition, Data curation. **Jonathan D. Gilthorpe:** Writing – review & editing, Validation, Resources, Investigation, Funding acquisition, Data curation. **Farhan Shah:** Writing – review & editing, Writing – original draft, Visualization, Validation, Supervision, Software, Resources, Project administration, Methodology, Investigation, Funding acquisition, Formal analysis, Data curation, Conceptualization.

Ethics approval and consent to participate

The Regional Medical Ethical Committee in Umeå approved the study (Dnr-05–130 M). Patients and voluntary control subjects were informed about the research project and acquisition of biopsies and gave their written consent to participate. All muscle samples were collected in agreement with the Declaration of Helsinki.

Availability of data and materials

The mass spectrometry proteomics datasets generated and analysed during the current study have been deposited to the ProteomeXchange Consortium via the PRIDE partner repository with the dataset identifier PXD064615 (Username: reviewer_pxd064615@ebi.ac.uk, Password: vr7iXuF6OqmB). The human datasets used and analysed during the current study are available from the corresponding author on reasonable request.

Funding

This work was supported by funding from the Swedish Research Council (Vetenskapsrådet 2018-02574, Per Stål) and Kempestiftelserna (JCSMK23-0001 and JCSMK25-0083, Farhan Shah) Cancerforskningsfonden I Norrland (AMP 25–1203, Farhan Shah). The Seahorse Platform at Umeå University was funded by ALF-investment award for medical and technical equipment (VLL-504771 and VLL-59531), Kempestiftelserna (JCK-1526 and KCK-1620) and Medical Faculty at Umeå University (Jonathan D. Gilthorpe). Mass spectrometry-based proteomics analysis was enabled by funding from Kempestiftelserna (JCK3126, Andre Mateus).

Declaration of competing interest

The authors declare that they have no known competing financial interests or personal relationships that could have appeared to influence the work reported in this paper.

Acknowledgements

We thank Anna-Karin Olofsson for her excellent technical assistance and Roger Widmark, Anders Bäckström, and Per Utsi for their invaluable assistance in the design, construction, and software-based analysis of the in vitro snoring vibration model. We also thank Associate Professor Thorbjörn Holmlund for performing clinical procedures and investigations.

References

Shah, F., Holmlund, T., Jäghagen, E.L., Berggren, D., Franklin, K., Forsgren, S., et al., 2018. Axon and Schwann cell degeneration in nerves of upper airway relates to pharyngeal dysfunction in snorers and patients with sleep apnea. Chest 30 (18), 30963–30972.

Friberg, D., Ansved, T., Borg, K., Carlsson-Nordlander, B., Larsson, H., Svanborg, E., 1998. Histological indications of a progressive snorers disease in an upper airway muscle. Am. J. Respir. Crit. Care Med. 157 (2), 586–593.

Boyd, J.H., Petrof, B.J., Hamid, Q., Fraser, R., Kimoff, R.J., 2004. Upper airway muscle inflammation and denervation changes in obstructive sleep apnea. Am. J. Respir. Crit. Care Med. 170 (5), 541–546. https://doi.org/10.1164/rccm.200308-1100OC. Epub 2004 May 19.

Bovenzi, M., 2005. Health effects of mechanical vibration. G. Ital. Med. Lav. Ergon. 27 (1), 58–64.

Murfee WL, Hammett LA, Evans C, Xie L, Squire M, Rubin C, et al. High-frequency, low-magnitude vibrations suppress the number of blood vessels per muscle fiber in mouse soleus muscle. J Appl Physiol (1985). 2005;98(6):2376-80. Epub 005 Jan 27.

Necking, L.E., Lundborg, G., Lundstrom, R., Thornell, L.E., Friden, J., 2004. Hand muscle pathology after long-term vibration exposure. J Hand Surg Br. 29 (5), 431–437.

Waugh, S., Kashon, M.L., Li, S., Miller, G.R., Johnson, C., Krajnak, K., 2016. Transcriptional pathways altered in response to vibration in a model of hand-arm vibration syndrome. J. Occup. Environ. Med. 58 (4), 344–350.

Silver, J., Wadley, G., Lamon, S., 2018. Mitochondrial regulation in skeletal muscle: a role for non-coding RNAs? Exp. Physiol. 103 (8), 1132–1144.

Ishihara, T., Ban-Ishihara, R., Maeda, M., Matsunaga, Y., Ichimura, A., Kyogoku, S., et al., 2015. Dynamics of mitochondrial DNA nucleoids regulated by mitochondrial fission is essential for maintenance of homogeneously active mitochondria during neonatal heart development. Mol. Cell Biol. 35 (1), 211–223.

Chen, W., Zhao, H., Li, Y., 2023. Mitochondrial dynamics in health and disease: mechanisms and potential targets. Signal Transduct. Target. Ther. 8 (1), 333.

Yapa, N.M.B., Lisnyak, V., Reljic, B., Ryan, M.T., 2021. Mitochondrial dynamics in health and disease. FEBS Lett. 595 (8), 1184–1204.

Wheaton, W.W., Hypoxia, C.NS., 2011. 2. Hypoxia regulates cellular metabolism. Am. J. Physiol. Cell Physiol. 300 (3), C385–C393.

Mungai, P.T., Waypa, G.B., Jairaman, A., Prakriya, M., Dokic, D., Ball, M.K., et al., 2011. Hypoxia triggers AMPK activation through reactive oxygen species-mediated activation of calcium release-activated calcium channels. Mol. Cell Biol. 31 (17), 3531–3545.

Jäghagen, E.L., Berggren, D., Isberg, A., 2000. Swallowing dysfunction related to snoring: a videoradiographic study. Acta Otolaryngol. 120 (3), 438–443.

Krajnak, K., 2020. Frequency-dependent changes in mitochondrial number and generation of reactive oxygen species in a rat model of vibration-induced injury. J. Toxic. Environ. Health A 83 (1), 20–35.

Curry, B.D., Bain, J.L., Yan, J.G., Zhang, L.L., Yamaguchi, M., Matloub, H.S., et al., 2002. Vibration injury damages arterial endothelial cells. Muscle Nerve 25 (4), 527–534.

Hughes, C.S., Foehr, S., Garfield, D.A., Furlong, E.E., Steinmetz, L.M., Krijgsveld, J., 2014. Ultrasensitive proteome analysis using paramagnetic bead technology. Mol. Syst. Biol. 10 (10), 757.

Hughes, C.S., Moggridge, S., Müller, T., Sorensen, P.H., Morin, G.B., Krijgsveld, J., 2019. Single-pot, solid-phase-enhanced sample preparation for proteomics experiments. Nat. Protoc. 14 (1), 68–85.

Huber, W., von Heydebreck, A., Sültmann, H., Poustka, A., Vingron, M., 2002. Variance stabilization applied to microarray data calibration and to the quantification of differential expression. Bioinformatics 18 (Suppl 1), S96–S.

Raudvere, U., Kolberg, L., Kuzmin, I., Arak, T., Adler, P., Peterson, H., et al., 2019. g: Profiler: a web server for functional enrichment analysis and conversions of gene lists (2019 update). Nucleic Acids Res. 47 (W1), W191–W198.

Shah, F., Berggren, D., Holmlund, T., Levring Jäghagen, E., Stål, P., 2016. Unique expression of cytoskeletal proteins in human soft palate muscles. J. Anat. 228 (3), 487–494. https://doi.org/10.1111/joa.12417. Epub 2015 Nov 24.

Walker, J.E., 2013. The ATP synthase: the understood, the uncertain and the unknown. Biochem. Soc. Trans. 41 (1), 1–16.

Guerrero-Castillo, S., Baertling, F., Kownatzki, D., Wessels, H.J., Arnold, S., Brandt, U., et al., 2017. The assembly pathway of mitochondrial respiratory chain complex I. Cell Metab. 25 (1), 128–139.

Hynes, R.O., 2002. Integrins: bidirectional, allosteric signaling machines. Cell 110 (6), 673–687.

Sun, Z., Guo, S.S., Fässler, R., 2016. Integrin-mediated mechanotransduction. J. Cell Biol. 215 (4), 445–456.

Coste, B., Mathur, J., Schmidt, M., Earley, T.J., Ranade, S., Petrus, M.J., et al., 2010. Piezo1 and Piezo2 are essential components of distinct mechanically activated cation channels. Science 330 (6000), 55–60.

Syeda, R., Florendo, M.N., Cox, C.D., Kefauver, J.M., Santos, J.S., Martinac, B., et al., 2016. Piezo1 channels are inherently mechanosensitive. Cell Rep. 17 (7), 1739–1746.

Mitra, S.K., Hanson, D.A., Schlaepfer, D.D., 2005. Focal adhesion kinase: in command and control of cell motility. Nat. Rev. Mol. Cell Biol. 6 (1), 56–68.

Geiger, B., Spatz, J.P., Bershadsky, A.D., 2009. Environmental sensing through focal adhesions. Nat. Rev. Mol. Cell Biol. 10 (1), 21–33.

Vogel, C., Marcotte, E.M., 2012. Insights into the regulation of protein abundance from proteomic and transcriptomic analyses. Nat. Rev. Genet. 13 (4), 227–232.

Ingber, D.E., 2006. Cellular mechanotransduction: putting all the pieces together again. FASEB J. 20 (7), 811–827.

Youle, R.J., van der Bliek, A.M., 2012. Mitochondrial fission, fusion, and stress. Science 337 (6098), 1062–1065.

Levring Jäghagen, E., Franklin, K.A., Isberg, A., 2003. Snoring, sleep apnoea and swallowing dysfunction: a videoradiographic study. Dentomaxillofac. Radiol. 32 (5), 311–316.

Liesa, M., Shirihai, O.S., 2013. Mitochondrial dynamics in the regulation of nutrient utilization and energy expenditure. Cell Metab. 17 (4), 491–506.

Tait, S.W., Green, D.R., 2010. Mitochondria and cell death: outer membrane permeabilization and beyond. Nat. Rev. Mol. Cell Biol. 11 (9), 621–632.

Galluzzi, L., Vitale, I., Aaronson, S.A., Abrams, J.M., Adam, D., Agostinis, P., et al., 2018. Molecular mechanisms of cell death: recommendations of the Nomenclature Committee on Cell Death 2018. Cell Death Differ. 25 (3), 486–541.

Mor, I., Cheung, E.C., Vousden, K.H., 2011. Control of glycolysis through regulation of PFK1: old friends and recent additions. Cold Spring Harb. Symp. Quant. Biol. 76, 211–216.

Kunji, E.R.S., King, M.S., Ruprecht, J.J., Thangaratnarajah, C., 2020. The SLC25 carrier family: important transport proteins in mitochondrial physiology and pathology. Physiology (Bethesda) 35 (5), 302–327.

Kunji, E.R., Aleksandrova, A., King, M.S., Majd, H., Ashton, V.L., Cerson, E., et al., 2016. The transport mechanism of the mitochondrial ADP/ATP carrier. Biochim. Biophys. Acta 1863 (10), 2379–2393.

Voos, W., 2013. Chaperone-protease networks in mitochondrial protein homeostasis. Biochim. Biophys. Acta 1833 (2), 388–399.

Wilkinson, M.E., Charenton, C., Nagai, K., 2020. RNA splicing by the spliceosome. Annu. Rev. Biochem 89, 359–388.

Zhou, Z., Fu, X.D., 2013. Regulation of splicing by SR proteins and SR protein-specific kinases. Chromosoma 122 (3), 191–207.

Wang, F., Zhang, D., Zhang, D., Li, P., Gao, Y., 2021. Mitochondrial protein translation: emerging roles and clinical significance in disease. Front. Cell Dev. Biol. 9, 675465.

Wahl, M.C., Will, C.L., Lührmann, R., 2009. The spliceosome: design principles of a dynamic RNP machine. Cell 136 (4), 701–718.

Dvinge, H., Guenthoer, J., Porter, P.L., Bradley, R.K., 2019. RNA components of the spliceosome regulate tissue- and cancer-specific alternative splicing. Genome Res. 29 (10), 1591–1604.

Scotti, M.M., Swanson, M.S., 2016. RNA mis-splicing in disease. Nat. Rev. Genet. 17 (1), 19–32.

Shah, F., Forsgren, S., Holmlund, T., Levring Jaghagen, E., Berggren, D., Franklin, K.A., et al., 2019. Neurotrophic factor BDNF is upregulated in soft palate muscles of snorers and sleep apnea patients. Laryngoscope Investig Otolaryngol. 4 (1), 174–180.

Shah, F., Franklin, K.A., Holmlund, T., Levring Jäghagen, E., Berggren, D., Forsgren, S., et al., 2019. Desmin and dystrophin abnormalities in upper airway muscles of snorers and patients with sleep apnea. Respir. Res. 20 (1), 31. https://doi.org/10.1186/s12931-019-0999-9.

Stål, P.S., Johansson, B., 2012. Abnormal mitochondria organization and oxidative activity in the palate muscles of long-term snorers with obstructive sleep apnea. Respiration Int. Rev. Thoracic Dis. 83 (5), 407–417. https://doi.org/10.1159/000336040. Epub 2012 Mar 1.

Stål, P., Nord, H., von Hofsten, J., Holmlund, T., Shah, F., 2024. Desmin gene expression is not ubiquitous in all upper airway myofibers and the pattern differs between healthy and sleep apnea subjects. Eur. J. Med. Res. 29 (1), 216.

Clemen, C.S., Herrmann, H., Strelkov, S.V., Schroder, R., 2013. Desminopathies: pathology and mechanisms. Acta Neuropathol. 125 (1), 47–75. https://doi.org/10.1007/s00401-012-1057-6. Epub 2012 Nov 11.

Smolina, N., Khudiakov, A., Knyazeva, A., Zlotina, A., Sukhareva, K., Kondratov, K., et al., 2020. Desmin mutations result in mitochondrial dysfunction regardless of their aggregation properties. Biochim. Biophys. Acta Mol. basis Dis. 1866 (6), 165745.

Agnetti G, Herrmann H, Cohen S. New roles for desmin in the maintenance of muscle homeostasis. FEBS J. 2022 May;289(10):2755-2770. doi: 10.1111/febs.15864. Epub 2021 Apr 22. PMID: 33825342.